Interaction between mountain waves and shear flow in an inertial layer

Jin-Han Xie[1] **and Jacques Vanneste**[2]

[1] Department of Physics, University of California, Berkeley, CA 94720, USA

[2] School of Mathematics and Maxwell Institute for Mathematical Sciences, University of Edinburgh, Edinburgh EH9 3JZ, UK

(Received xx; revised xx; accepted xx)

Mountain-generated inertia-gravity waves (IGWs) affect the dynamics of both the atmosphere and the ocean through the mean force they exert as they interact with the flow. A key to this interaction is the presence of critical-level singularities or, when planetary rotation is taken into account, inertial-level singularities, where the Doppler-shifted wave frequency matches the local Coriolis frequency. We examine the role of the latter singularities by studying the steady wavepacket generated by a multiscale mountain in a rotating linear shear flow at low Rossby number. Using a combination of WKB and saddle-point approximations, we provide an explicit description of the form of the wavepacket, of the mean forcing it induces, and of the mean-flow response.

We identify two distinguished regimes of wave propagation: Regime I applies far enough from a dominant inertial level for the standard ray-tracing approximation to be valid; Regime II applies to a thin region where the wavepacket structure is controlled by the inertial-level singularities. The wave–mean-flow interaction is governed by the change in Eliassen–Palm (or pseudomomentum) flux. This change is localised in a thin inertial layer where the wavepacket takes a limiting form of that found in Regime II. We solve a quasi-geostrophic potential-vorticity equation forced by the divergence of the Eliassen–Palm flux to compute the wave-induced mean flow. Our results, obtained in an inviscid limit, show that the wavepacket reaches a large-but-finite distance downstream of the mountain (specifically, a distance of order $k_*^{1/2}\Delta^{3/2}$, where k_*^{-1} and Δ measure the wave and envelope scales of the mountain) and extends horizontally over a similar scale.

1. Introduction

The importance of mountain-generated inertia-gravity waves for the atmospheric circulation has long been recognised (see Fritts & Alexander 2003, for a review), and their parameterisation is now an essential element of weather-forecasting and climate models (e.g., Alexander *et al.* 2010). Their oceanic counterparts, while often neglected, are now increasingly thought to play a significant role for the oceanic circulation (e.g. Scott *et al.* 2011; Nikurashin & Ferrari 2011, 2013). These waves impact both the atmospheric and oceanic circulations through the drag they extert where they dissipate, often through their interaction with the large-scale flow at critical levels where the mean flow velocity vanishes or, accounting for the background rotation, at inertial levels where their Doppler-shifted frequency matches the local Coriolis frequency.

Our understanding of this form of interaction with the mean flow rests on a number of now classical papers (including Eliassen & Palm 1961; Bretherton 1966, 1969*a*,*b*; Jones 1967; Booker & Bretherton 1967) that tackled both the propagation of the waves in a shear flow and the drag they exert on the flow. These identified the Eliassen–Palm (EP) flux (or pseudomomentum flux) as the key quantity controlling the drag, showed that

its conservation in the absence of dissipation leads to non-interaction results (Charney & Drazin 1961; Andrews & McIntyre 1976, 1978), and elucidated how critical-level and inertial-level singularities disrupt this conservation and result in drag. These results have subsequently been applied to a variety of mountain shapes and flows.

The present paper focusses on the case of a topographic profile with two well-separated horizontal scales, with small-scale oscillations modulated over a large envelope scale. Topographies of this form are assumed in atmospheric-model parameterisations (Martin & Lott 2007) and are natural for the ocean, e.g., in ridge regions. Our aim is to provide a detailed description of the wavepacket generated by a relatively weak flow whose Rossby number based on the envelope scale is small. The Rossby number based on the oscillation scale is however large enough for the waves to be vertically propagating (rather than evanescent) from the ground up. The flow considered is back sheared, with a zero-velocity, critical level above the ground. In this setup, background rotation is crucial in two respects: first, it contributes to the dispersion relation; second, it determines the nature of the singularities in the vertical structure of the wave solution. Specifically, rotation resolves the degeneracy of the critical level singularity, which is independent of wavenumber, into a pair of wavenumber-dependent inertial levels. As a result, the singularities associated with the broad wavenumber spectrum of a wavepacket are smeared out over a range of altitude – the inertial layer – and the wavepacket solution itself is smooth in the limit of vanishing dissipation (Shutts 2001). (An analogous effect arises when the orientation of the flow changes with altitude, see Shutts (1995, 2003).)

We tackle the three essential aspects of the problem by computing (i) the shape of the wavepacket, (ii) the associated EP flux, and (iii) the mean-flow change that results from the divergence of this EP flux. We take advantage of the assumption of small Rossby number and of a related assumption of large Richardson number to carry out the entire computation asymptotically, relying on the WKB form of the vertical structure of plane waves in the horizontal obtained by Lott *et al.* (2010, 2012). The analysis identifies two distinct altitude ranges corresponding to two distinct asymptotic regimes. In the first, valid away from the inertial levels, standard ray tracing applies and the (horizontally integrated) EP flux is independent of altitude; in the second, valid in a thin region surrounding the inertial layer, the solution is more complicated and captures the finiteness of the wavepacket deflection as it approaches a central inertial level. It turns out that inertial-level absorption affects only a still thinner region, which defines an inertial layer. The mean drag is vertically localised in this layer.

The asymptotic approach provides answers to basic questions – such as the horizontal distance between mountain and region of wave drag, and the extent of this region – as scaling laws in terms of key parameters characterising the stratification, shear and mountain shape. These scaling relations, which likely apply to more general setups than the one we consider, may prove useful for the representation of moutain-wave drag in numerical models.

The structure of this paper is as follows. We formulate the problem in §2 and approximate the form of the wavepacket in different regimes using a steepest-descent method in §3. In §4 we use this approximation to calculate the EP flux and solve a mean quasi-geostrophic potential-vorticity equation to obtain the mean-flow response. We summarise and discuss our results in §5.

2. Formulation

We consider the interaction between a steady topographic wavepacket and a background shear flow in an idealized setup shown in Fig. 1. The background flow is chosen

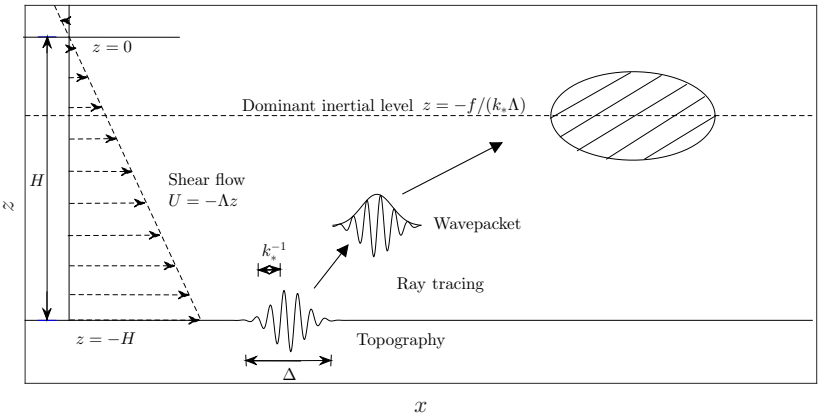

FIGURE 1. Schematic representation of the setup of the problem in the (x, z)-plane. A wavepacket generated by a two-scale mountain at the ground $z = -H$ propagates vertically in the shear flow $\boldsymbol{U} = (-\Lambda z, 0)$ and drives a mean-flow in the (hatched) region localised around the dominant inertial level $z = -f/(k_*\Lambda)$.

as a unidirectional, uniform backward shear flow $\boldsymbol{U} = (-\Lambda z, 0, 0)$ with $\Lambda = \text{const.} > 0$. The distance between the level of zero background velocity (critical level) and the bottom boundary is H. It proves convenient to use a slightly unusual vertical coordinate such that $z = 0$ and $z = -H$ correspond to the critical level and ground, respectively. The topographic wavepacket is generated by an idealized multiscale mountain with height

$$\begin{aligned} h_{\mathrm{t}}(x, y) &= h\,\mathrm{Re}\left(\mathrm{e}^{-(x^2+y^2)/(2\Delta^2)}\mathrm{e}^{\mathrm{i}\boldsymbol{k}_*\cdot\boldsymbol{x}}\right) \\ &= \frac{\Delta^2 h}{2\pi}\mathrm{Re}\left(\int_{-\infty}^{\infty}\int_{-\infty}^{\infty}\mathrm{e}^{-|\boldsymbol{k}-\boldsymbol{k}_*|^2\Delta^2/2}\mathrm{e}^{\mathrm{i}\boldsymbol{k}\cdot\boldsymbol{x}}\mathrm{d}k\mathrm{d}l\right), \end{aligned} \tag{2.1}$$

where $\boldsymbol{x} = (x, y)$, $\boldsymbol{k} = (k, l)$, $\boldsymbol{k}_* = (k_*, l_*)$ is the dominant wavevector, h is the maximum height of the mountain, and Re denotes the real part. Here k_*^{-1} and Δ control the oscillation scale and envelope scale of the moutain so that the parameter $k_*\Delta \gg 1$ characterizes the separation between these scales.

The fluid satisfies the f-plane hydrostatic Boussinesq equations

$$\partial_t\boldsymbol{u} + \boldsymbol{u}\cdot\nabla\boldsymbol{u} + w\partial_z\boldsymbol{u} + f\boldsymbol{e}_z\times\boldsymbol{u} = -\nabla\phi, \tag{2.2a}$$

$$\partial_z\phi = b, \tag{2.2b}$$

$$\partial_t b + \boldsymbol{u}\cdot\nabla b + w\partial_z b + N^2 w = 0, \tag{2.2c}$$

$$\nabla\cdot\boldsymbol{u} + \partial_z w = 0, \tag{2.2d}$$

where $\boldsymbol{u} = (u, v)$ is the horizontal velocity, w the vertical velocity, ϕ a scaled pressure, b the buoyancy, f the local Coriolis frequency, $\boldsymbol{e}_z$ the unit vertical vector pointing upwards, N the Brunt-Väisälä frequency, taken to be a constant, and $\nabla = (\partial_x, \partial_y)$ is the horizontal gradient.

We apply a no-normal flow boundary condition at the lower boundary:

$$w = \boldsymbol{u}_{\mathrm{b}}\cdot\nabla h_{\mathrm{t}} \quad \text{at} \quad z = -H + h_{\mathrm{t}}, \tag{2.3}$$

where the subscript "b" denotes the value on the boundary.

3. Wave solution

3.1. *Preliminaries*

We examine small-amplitude waves governed by the linearization of the primitive equations (2.2) about the background flow. This is in geostrophic balance and given by

$$U_0 = -\partial_y \Psi_0, \quad V_0 = 0, \quad W_0 = 0, \quad B_0 = f\partial_z \Psi_0, \quad \Phi_0 = f\Psi_0, \quad \text{where} \quad \Psi_0 = \Lambda yz. \tag{3.1}$$

We assume a small Rossby number based on the envelope scale Δ of the topography:

$$\mathrm{Ro} = \frac{U_\mathrm{b}}{f\Delta} \ll 1, \tag{3.2}$$

where $U_\mathrm{b} = \Lambda H$. We are interested in propagating mountain waves, in the distinguished regime where the Doppler-shifted frequency $U_\mathrm{b}k_*$ is of the same order as the Coriolis frequency. This corresponds to the scaling

$$k_*\Delta = O(\mathrm{Ro}^{-1}) \gg 1, \tag{3.3}$$

which we assume. The waves are propagating and not evanescent at the bottom boundary provided that $U_b k_* > f$ or, equivalently,

$$k_*\Delta\mathrm{Ro} > 1, \tag{3.4}$$

which we also assume.

Linearizing (2.2) around the background flow (3.1) leads to the equations

$$\partial_t \boldsymbol{u}_1 - \Lambda z\partial_x \boldsymbol{u}_1 + \Lambda w_1 \boldsymbol{e}_x + f\boldsymbol{e}_z \times \boldsymbol{u}_1 = -\nabla\phi_1, \tag{3.5a}$$

$$\partial_z \phi_1 = b_1, \tag{3.5b}$$

$$\partial_t b_1 - \Lambda z\partial_x b_1 + f\Lambda v_1 + N^2 w_1 = 0, \tag{3.5c}$$

$$\nabla\cdot\boldsymbol{u}_1 + \partial_z w_1 = 0. \tag{3.5d}$$

with $\boldsymbol{e}_x$ the unit vector in the x-direction, which govern the leading-order wave fields, denoted here by the subscript "1". The amplitude of the waves is determined by the linearisation of the boundary condition (2.3),

$$w_1 = U_\mathrm{b}\partial_x h_\mathrm{t}. \tag{3.6}$$

This indicates that $w_1 = O(U_\mathrm{b}k_*h)$. The polarization relation for standard internal waves (see also (3.12a) below) can then be used to estimate $u_1 = O(Nw_1/(k_*U_\mathrm{b})) = O(Nh)$. The linearization based on the small-amplitude condition $u_1 \ll U_\mathrm{b}$ thus requires that the inverse Froude number

$$\frac{Nh}{U_\mathrm{b}} = J\frac{h}{H} \ll 1, \tag{3.7}$$

where $J = N/\Lambda = \mathrm{Ri}^{1/2}$, with $\mathrm{Ri} = N^2/\Lambda^2$ the Richardson number. Based on this small parameter, we introduce the convention of using a subscript 'n' ($n = 1, 2, 3\ldots$) to denote the nth-order flow variables such that

$$u_n = O\left(\left(J\frac{h}{H}\right)^n U_\mathrm{b}\right). \tag{3.8}$$

After applying a Fourier transform, (3.5) can be reduced to the single equation

$$\frac{1-\zeta^2}{\zeta^2}\hat{w}_{\zeta\zeta} - \left(\frac{2}{\zeta^3} - \frac{2\mathrm{i}\nu}{\zeta^2}\right)\hat{w}_\zeta - \left(\frac{(1+\nu^2)J^2}{\zeta^2} + \frac{2\mathrm{i}\nu}{\zeta^3}\right)\hat{w} = 0, \tag{3.9}$$

where $\nu = l/k$. (This is equation (25) in Jones (1967) and equation (4) in Yamanaka & Tanaka (1984).) The independent variable is the scaled vertical coordinate

$$\zeta = -k\Lambda z/f. \tag{3.10}$$

We emphasise that for $k > 0$, as will be assumed when interpreting the results, ζ has a sign opposite to that of z and is positive below the inertial level and increasing downwards. The dependent variable $\hat{w}$ is the horizontal Fourier transform of w_1, defined by

$$w_1 = \frac{1}{2\pi}\int_{-\infty}^{\infty}\int_{-\infty}^{\infty} \hat{w}(k,l)\mathrm{e}^{\mathrm{i}\boldsymbol{k}\cdot\boldsymbol{x}}\,\mathrm{d}k\mathrm{d}l. \tag{3.11}$$

The other dependent variables are related to $\hat{w}$ through the polarization relations

$$\hat{u} = \mathrm{i}\frac{-\Lambda}{f}\left(\frac{\zeta - \mathrm{i}\nu}{\zeta(1+\nu^2)}\hat{w}_\zeta + \frac{\nu^2}{\zeta(1+\nu^2)}\hat{w}\right), \tag{3.12a}$$

$$\hat{v} = \frac{\Lambda}{f}\left(\frac{1 - \mathrm{i}\nu\zeta}{\zeta(1+\nu^2)}\hat{w}_\zeta + \frac{\mathrm{i}\nu}{\zeta(1+\nu^2)}\hat{w}\right), \tag{3.12b}$$

$$\hat{b} = \mathrm{i}\frac{\Lambda^2}{f}\left(\frac{1 - \mathrm{i}\nu\zeta}{\zeta^2(1+\nu^2)}\hat{w}_\zeta + \left(\frac{\mathrm{i}\nu}{\zeta^2(1+\nu^2)} + \frac{J^2}{\zeta}\right)\hat{w}\right). \tag{3.12c}$$

One of the key characteristics of IGWs in shear flow is the presence of singularities: two inertial levels, where the Doppler-shifted frequency matches the Coriolis frequency, and a critical level, where the Doppler-shifted frequency and hence the background velocity vanish (Jones 1967). These singularities are readily identified from (3.9): the two inertial levels and one critical level correspond to $\zeta = \pm 1$ and $\zeta = 0$, respectively. The critical level is an apparent singularity that can be removed by a variable transformation. The inertial levels, by contrast, have a marked physical impact since the wave solution switches abruptly from an oscillatory to an evanescent behaviour and back across them (Yamanaka & Tanaka 1984; Lott *et al.* 2015). As we discuss in §4, this abrupt change underpins the forcing of a mean flow by the wavepacket.

Rotation plays a crucial role. The position $z = \pm f/(k\Lambda)$ of the inertial levels depends on the wavenumber k; as a result, the singularities associated with each wavenumber making up the wavepacket are smeared out over a range of altitude, and the wavepacket solution is smooth even in the absence of dissipation (or more precisely in the limit of vanishing dissipation since dissipation is important to determine physically relevant branches of solution; Shutts 2001). This is in contrast with the non-rotating scenario, best thought of as the limit $f \to 0$ of the general situation. In this limit, the inertial levels coalesce with the critical level, leading to a stronger, k-independent singularity and to a singular behaviour of the wavepacket unless dissipation is introduced. (A similar smearing out of singularities across different altitudes also occurs without rotation when more complicated flows, such as the directional shear flow, are considered; Shutts 1995, 2003, Martin & Lott 2007.)

The term 'inertial layer' is used to describe the region where the effect of the inertial-level singularities is distributed. It is centred around the dominant inertial level,

$$z_* = -\frac{f}{k_*\Lambda}, \tag{3.13}$$

determined by the central wavenumber k_* of the topography. Note that, for the problem under consideration, only the lower inertial levels matter since the waves are exponentially small in J at the upper inertial levels. Condition (3.4) ensures that $z_* > -H$, that is, the dominant inertial level lies in the fluid domain. The characteristic thickness of the

inertial layer is found as

$$\delta_* = -\frac{z_*}{k_*}\delta k = \frac{f}{k_*^2 \Lambda \Delta}, \tag{3.14}$$

on using that, according to expression (2.1) for the mountain height, the spectral width of the wavepacket is $\delta k = \Delta^{-1}$.

Equation (3.9) for $\hat{w}$ can be solved explicitly in terms of hypergeometric functions (Yamanaka & Tanaka 1984; Shutts 2001). We rely instead on the approximate WKB solution derived in Lott *et al.* (2012) (see also Lott *et al.* (2015)) and valid in the large-Richardson limit $J \gg 1$. For simplicity, we adopt the scaling

$$J = O(\mathrm{Ro}^{-1}) \gg 1. \tag{3.15}$$

Together with (3.3), this implies that $NH/(f\Delta) = O(1)$, corresponding to an order-one Burger number based on the horizontal and vertical scales Δ and H. In the WKB approximation, $\hat{w}$ is given by

$$\hat{w} = \frac{\zeta}{\zeta_\mathrm{b}} \left(\frac{\zeta_\mathrm{b}-1}{\zeta-1}\right)^{1/4-\mathrm{i}\nu/2} \left(\frac{\zeta_\mathrm{b}+1}{\zeta+1}\right)^{1/4+\mathrm{i}\nu/2} \mathrm{e}^{-\mathrm{i}J\sqrt{1+\nu^2}D(\zeta)}, \tag{3.16}$$

where

$$D(\zeta) = \ln(\zeta + \sqrt{\zeta^2-1}) - \ln(\zeta_\mathrm{b} + \sqrt{\zeta_\mathrm{b}^2-1}), \quad \text{with} \quad \zeta_\mathrm{b} = k\Lambda H/f. \tag{3.17}$$

Note that we have normalized $\hat{w}$ so that its bottom-boundary value is $\hat{w}(\zeta_\mathrm{b}) = 1$.

Expression (3.16) holds for all real values of ζ except in small regions of $O(J^{-2})$ thickness around the inertial levels $\zeta = \pm 1$, provided that suitable branches of the multivalued functions are chosen (see Jones (1967); Lott *et al.* (2012, 2015)). The sign of the argument of the exponential is taken to be negative; this ensures that the wave is propagating upwards above the upper inertial level, that is, for $\zeta < -1$ (see Booker & Bretherton (1967); note that the opposite, positive sign is found when the background velocity is increasing with altitude). The multivalued functions are continued from $\zeta > 1$ to $\zeta < -1$ along a contour in the complex plane that passes below the singularities at $\zeta = \pm 1$. In this way, the solution is decreasing exponentially with ζ between the inertial level (like $\exp(-J\sqrt{1+\nu^2}\cos^{-1}\zeta)$) and experiences an overall absorption by the factor $\exp(-J\sqrt{1+\nu^2}\pi)$ known to apply to both the rotating and non-rotating cases (Booker & Bretherton 1967; Jones 1967; Lott *et al.* 2015). The choice of continuation is dictated by considerations of causality which are readily settled by adding small damping terms in (3.5). It is in this sense that the problem is not treated as strictly inviscid but rather as a vanishing viscosity limit.

The WKB approximation (3.16) breaks down near the inertial levels, specifically for $||\zeta|-1| = O(J^{-2})$ where it should be replaced by an expression in terms of Hankel functions (Lott *et al.* 2012). These regions are narrow enough and the singularities of (3.16) at $\zeta = \pm 1$ are mild enough that they can be ignored when computing the vertical velocity of the complete wavepacket.

Substituting the form (2.1) of the topography into the boundary condition (3.6), we obtain the vertical velocity at the boundary as the Fourier expansion

$$w_\mathrm{1b} = \frac{\mathrm{i}U_\mathrm{b}h\Delta^2}{2\pi} \int_{-\infty}^{\infty}\int_{-\infty}^{\infty} k\mathrm{e}^{-|\boldsymbol{k}-\boldsymbol{k}_*|^2\Delta^2/2}\mathrm{e}^{\mathrm{i}\boldsymbol{k}\cdot\boldsymbol{x}}\,\mathrm{d}k\mathrm{d}l. \tag{3.18}$$

Here and henceforth, a real part is implied. Combining this with (3.11) and (3.16) leads

to the vertical velocity of the wavepacket in the form

$$w_1 = \frac{\mathrm{i}U_\mathrm{b}h\Delta^2}{2\pi}\int_{-\infty}^{\infty}\int_{-\infty}^{\infty} k\mathrm{e}^{-|\boldsymbol{k}-\boldsymbol{k}_*|^2\Delta^2/2}\hat{w}\,\mathrm{e}^{\mathrm{i}\boldsymbol{k}\cdot\boldsymbol{x}}\,\mathrm{d}k\mathrm{d}l. \tag{3.19}$$

Note that, because $\hat{w}$ is exponentially small for $\zeta < 1$ as a result of wave absorption, the lower limit of the integral in k could be taken as $-f\Lambda^{-1}z^{-1}$. This absorption is crucial for the impact of the wavepacket on the mean flow.

3.2. *Saddle-point approximations*

The solution (3.19) can be further simplified by taking advantage of the assumptions $J \gg 1$ and $k_*\Delta \gg 1$ to apply a saddle-point approximation. The key is to identify the dominant terms in the argument of the exponential, including a contribution from $\hat{w}$. To avoid defining several new dimensionless numbers measuring the relative size of J, $k_*\Delta$ and Ro, it is expedient to introduce a bookkeeping parameter ϵ which keeps track of the orders of various terms. This parameter is treated as formally small and used as a basis for a saddle-point approximation, but it is set to 1 at the end of the computation to obtain asymptotic formulas in a convenient dimensional form. The bookkeeping parameter ϵ is introduced through the replacements

$$k_*\Delta \mapsto \epsilon^{-1}k_*\Delta, \quad J \mapsto \epsilon^{-1}J \quad \text{and} \quad \mathrm{Ro} \mapsto \epsilon\mathrm{Ro}, \tag{3.20}$$

in accordance with the scalings (3.3) and (3.15). Thus the formal smallness of ϵ captures at once the mountain scale separation, the large Richardson number, and the small Rossby number.

Introducing (3.20) into (3.19) leads to

$$w_1 = \frac{\mathrm{i}U_\mathrm{b}hk_*\Delta^2}{2\pi\epsilon}\int_{-\infty}^{\infty}\int_{-\infty}^{\infty} \mathrm{e}^{-|\boldsymbol{k}-\epsilon^{-1}\boldsymbol{k}_*|^2\Delta^2/2}\hat{w}\mathrm{e}^{\mathrm{i}\boldsymbol{k}\cdot\boldsymbol{x}}\,\mathrm{d}k\mathrm{d}l, \tag{3.21}$$

where

$$\hat{w} = \frac{\zeta}{\zeta_\mathrm{b}}\left(\frac{\zeta_\mathrm{b}-1}{\zeta-1}\right)^{1/4-\mathrm{i}\nu/2}\left(\frac{\zeta_\mathrm{b}+1}{\zeta+1}\right)^{1/4+\mathrm{i}\nu/2}\mathrm{e}^{-\mathrm{i}\epsilon^{-1}J\sqrt{1+\nu^2}D(\zeta)}, \tag{3.22}$$

and makes the dependence on ϵ explicit. In writing this expression, we have made a first approximation by replacing the wavenumber k outside the exponential functions by its leading-order approximation k_*. The error introduced is negligible as can be verified below once the size of the neighbourhood of k_* controlling the integral is estimated.

A second approximation is made in carrying out the integration with respect to l in (3.21). Because the integral is dominated by values of l near $\epsilon^{-1}l_*$, we write

$$l = \epsilon^{-1}l_* + L, \tag{3.23}$$

where $\epsilon L/l_* \ll 1$, leading to the following expressions

$$\nu = \frac{l_*}{\epsilon k}\left(1+\epsilon\frac{L}{l_*}\right), \tag{3.24}$$

$$\sqrt{1+\nu^2} = \sqrt{1+\left(\frac{l_*}{\epsilon k}\right)^2} + \epsilon\frac{l_*L}{\epsilon k\sqrt{(\epsilon k)^2+l_*^2}} + O\left(\left(\epsilon\frac{L}{l_*}\right)^2\right), \tag{3.25}$$

where ϵk is treated as $O(1)$ since k is close to $\epsilon^{-1}k_*$. Substituting these into (3.21) and

neglecting $O((\epsilon L/l_*)^2)$, we obtain

$$\begin{aligned} w_1 = \frac{\mathrm{i}U_\mathrm{b}hk_*\Delta^2}{2\pi\epsilon}\int_{-\infty}^{\infty}\int_{-\infty}^{\infty} &\mathrm{e}^{-(\Delta L)^2/2-\mathrm{i}Jl_*(\epsilon k)^{-1}((\epsilon k)^2+l_*^2)^{-1/2}D(\zeta)L+\mathrm{i}Ly}\mathrm{d}L \\ &\times \mathrm{e}^{-(k-\epsilon^{-1}k_*)^2\Delta^2/2}\frac{\zeta}{\zeta_\mathrm{b}}\left(\frac{\zeta_\mathrm{b}-1}{\zeta-1}\right)^{1/4-\mathrm{i}\nu_*/2}\left(\frac{\zeta_\mathrm{b}+1}{\zeta+1}\right)^{1/4+\mathrm{i}\nu_*/2} \\ &\times \mathrm{e}^{-\mathrm{i}J\epsilon^{-1}(1+l_*^2/(\epsilon k)^2)^{1/2}D(\zeta)+\mathrm{i}kx}\,\mathrm{d}k \\ \doteq \frac{U_\mathrm{b}hk_*\Delta}{\epsilon\sqrt{2\pi}}\int_{-\infty}^{\infty} &\mathrm{e}^{-\left(y-Jl_*(\epsilon k)^{-1}((\epsilon k)^2+l_*^2)^{-1/2}D(\zeta)\right)^2/(2\Delta^2)} \\ &\times \mathrm{e}^{-(k-\epsilon^{-1}k_*)^2\Delta^2/2}\frac{\zeta}{\zeta_\mathrm{b}}\left(\frac{\zeta_\mathrm{b}-1}{\zeta-1}\right)^{1/4-\mathrm{i}\nu_*/2}\left(\frac{\zeta_\mathrm{b}+1}{\zeta+1}\right)^{1/4+\mathrm{i}\nu_*/2} \\ &\times \mathrm{e}^{-\mathrm{i}J\epsilon^{-1}(1+l_*^2/(\epsilon k)^2)^{1/2}D(\zeta)+\mathrm{i}kx}\,\mathrm{d}k. \end{aligned} \tag{3.26}$$

In the second line, we have ignored a phase factor and introduced the symbol $\doteq$ to denote an equality in modulus only, ignoring phase factors. In what follows, we pay only attention to the modulus of w_1 since this controls the wave–mean flow interaction properties: the spatially averaged EP flux, which is quadratic in wave quantities, only depends on the wave amplitude and on the relative phase of various fields which is easily worked out.

The appearance of the bookkeeping parameter ϵ^{-1} in the exponential in (3.26) motivates the saddle-point approximation. To apply this, we need to compare the leading terms in the exponential, namely

$$(k-\epsilon^{-1}k_*)^2\Delta^2/2 \quad \text{and} \quad \mathrm{i}J\epsilon^{-1}\left(1+\left(\frac{l_*}{\epsilon k}\right)^2\right)^{1/2}D(\zeta). \tag{3.27}$$

The first term stems from the finite spectral width of the mountain height; the second term, which depends on ζ and hence z, captures the vertical structure of the wave. We seek distinguished regimes, where the leading-order terms in (3.27) balance. This requires approximating $D(\zeta)$ to determine its order, a non-trivial task since the order of $D(\zeta)$ depends on the value of ζ, that is, on the particular range of altitude considered. Mathematically, different altitude ranges are captured by different values of α in the scaling

$$z = z_*\left(1+\left(\frac{\epsilon}{k_*\Delta}\right)^\alpha Z\right), \tag{3.28}$$

where $Z = O(1)$.

Note that, since $z_* < 0$, Z and z have different signs, with $Z > 0$ below the dominant inertial level and increasing downwards. Because ζ depends on both z and k, we also need to scale k to find range of wavenumbers controlling the integral in (3.26). Since the wavepacket is concentrated around $\epsilon^{-1}k_*$, we write

$$k = \epsilon^{-1}k_*\left(1+\left(\frac{\epsilon}{k_*\Delta}\right)^\beta K\right), \quad \text{with} \quad K = O(1) \quad \text{and} \quad \beta \geqslant 0. \tag{3.29}$$

Combining (3.28) and (3.29), we obtain

$$\zeta = -\frac{k\Lambda z}{f} = 1+\left(\frac{\epsilon}{k_*\Delta}\right)^\beta K+\left(\frac{\epsilon}{k_*\Delta}\right)^\alpha Z+O\left(\left(\frac{\epsilon}{k_*\Delta}\right)^{\alpha+\beta}\right). \tag{3.30}$$

We now need to distinguish two situations: (i) for $\alpha = 0$, that is, away from the dominant

inertial level,

$$D(\zeta) = D(1+Z) + O\left(\left(\frac{\epsilon}{k_*\Delta}\right)^{\beta}\right); \tag{3.31}$$

(ii) for $\alpha > 0$, that is, asymptotically close to the dominant inertial level,

$$D(\zeta) = D(1) + O\left(\left(\frac{\epsilon}{k_*\Delta}\right)^{\min\{\alpha,\beta\}/2}\right). \tag{3.32}$$

Because the leading-order terms in these two expansions are independent of k, hence do not contribute to the integration over k in (3.26), the order of the second terms is crucial. Using the scalings of the second terms of (3.31)–(3.32) in the second expression in (3.27), and balancing with the first expression (scaling like $\epsilon^{2\beta-2}$) leads to two distinguished regimes: Regime I, with $\alpha = 0$ and $\beta = 1$, and Regime II, with $\alpha = \beta = 2/3$ (since $\alpha = \beta$ gives a distinguished regime). In each regime, the coordinate x appearing in $\exp(\mathrm{i}kx)$ should be scaled so that the K-dependent contribution to kx, proportional to $\epsilon^{\beta-1}$, be of the same order as the K-dependent terms in (3.27). This leads to $x = O(\Delta)$ in Regime I and $x = O(\epsilon^{-1/3}\Delta)$ in Regime II.

We carry out the saddle-point expansion of (3.26) in these two regimes in Appendix A and only quote the final results here. In Regime I, after setting $\epsilon = 1$, we find that

$$w_1 \doteq hf(1+Z_{\mathrm{I}})\left(\frac{(k_*\Delta)^2\mathrm{Ro}^2 - 1}{2Z_{\mathrm{I}} + Z_{\mathrm{I}}^2}\right)^{1/4} \mathrm{e}^{-\left(y - J\nu_* {k_*}^{-1}(1+\nu_*^2)^{-1/2} D_{\mathrm{I}}\right)^2/(2\Delta^2)} \mathrm{e}^{-X_{\mathrm{I}}^2/(2\Delta^2)}, \tag{3.33}$$

where

$$X_{\mathrm{I}} = x - \frac{J}{k_*}\left(\sqrt{1+\nu_*^2}\left(\frac{1+Z_{\mathrm{I}}}{\sqrt{2Z_{\mathrm{I}} + Z_{\mathrm{I}}^2}} - \frac{k_*\Delta\mathrm{Ro}}{\sqrt{(k_*\Delta)^2\mathrm{Ro}^2 - 1}}\right) - \frac{\nu_*^2}{\sqrt{1+\nu_*^2}} D_{\mathrm{I}}\right), \tag{3.34}$$

$D_{\mathrm{I}} = \ln(1 + Z_{\mathrm{I}} + \sqrt{2Z_{\mathrm{I}} + Z_{\mathrm{I}}^2}) - \ln(\zeta_{\mathrm{b}*} + \sqrt{\zeta_{\mathrm{b}*}^2 - 1})$, $Z_{\mathrm{I}} = z/z_* - 1$ and $\zeta_{\mathrm{b}*} = k_*\Lambda H/f$. This makes clear that the wavepacket retains the bell shape of topography, with scale Δ, throughout its propagation across Regime I. The path of the wavepacket in the (x,z)-plane is determined by setting $X_{\mathrm{I}} = 0$ in (3.33), which corresponds to standard ray tracing. It shows in particular that the wavepacket diverges to infinity as it approaches the dominant inertial level, with $x \sim Jk_*^{-1}(1+\nu_*^2)^{1/2}(2Z_{\mathrm{I}})^{-1/2}$ as $Z_{\mathrm{I}} \to 0$. This is a limitation of the approximation made in Regime I (also a limitation of ray tracing) rather than a physical effect as the analysis of Regime II shows.

In Regime II, and again with $\epsilon = 1$, we find that

$$w_1 \doteq \frac{U_{\mathrm{b}} h k_*^2 \Delta}{2^{1/4}\epsilon^{5/4}(k_*\Delta)^{3/4}} \frac{q(K_{\mathrm{s}})}{(p''(K_{\mathrm{s}}))^{1/2}} \mathrm{e}^{(k_*\Delta)^{2/3} p(K_{\mathrm{s}})} g(y), \tag{3.35}$$

where the y-dependence is controlled by the Gaussian

$$g(y) = \mathrm{e}^{-\left(y - J\nu_* {k_*}^{-1}(1+\nu_*^2)^{-1/2} D_{\mathrm{II}}\right)^2/(2\Delta^2)}, \tag{3.36}$$

with $D_{\mathrm{II}} = -\ln(\zeta_{\mathrm{b}*} + \sqrt{\zeta_{\mathrm{b}*}^2 - 1})$, and is decoupled from the dependence in x and z. In (3.35), the function p is defined by

$$p(K_{\mathrm{s}}) = -\frac{K_{\mathrm{s}}^2}{2} - \mathrm{i}J(k_*\Delta)\sqrt{1+\nu_*^2}\sqrt{2(K_{\mathrm{s}} + Z_{\mathrm{II}})} + \mathrm{i}K_{\mathrm{s}} X_{\mathrm{II}}, \tag{3.37}$$

and K_{s} is one of its saddle point, satisfying $p'(K_{\mathrm{s}}) = 0$, where the prime denotes

derivative. The other symbols introduced are

$$q(K_{\rm s}) = \frac{1}{(K_{\rm s}+Z_{\rm II})^{1/4}}, \tag{3.38}$$

$$X_{\rm II} = (k_*\Delta)^{-4/3}\left(k_*x + J\left(\frac{k_*\sqrt{1+\nu_*^2}\Delta{\rm Ro}}{\sqrt{(k_*\Delta)^2{\rm Ro}^2-1}} + \frac{\nu_*^2}{\sqrt{1+\nu_*^2}}D_{\rm II}\right)\right), \tag{3.39}$$

and $Z_{\rm II} = (k_*\Delta)^{2/3}(z/z_*-1)$. The saddle point $K_{\rm s}$ satisfies a cubic equation whose analytic solution is not particularly illuminating; we will solve it numerically. It is selected among the three roots of the cubic by the condition that it be accessible by a steepest-descent path connecting $-\infty$ to ∞. For large $Z_{\rm II}$, the expansion $\sqrt{2(K_{\rm s}+Z_{\rm II})} \sim \sqrt{2Z_{\rm II}} + K_{\rm s}/\sqrt{2Z_{\rm II}}$ can be used to confirm the matching between Regime I and Regime II. The behaviour for small $Z_{\rm II}$ is key for the mean-flow forcing. As discussed in §3.1, the change in EP flux is concentrated in the inertial layer, such that $|z-z_*| = O(\delta_*)$ with δ_* given in (3.14). This corresponds to the scaling

$$Z = \epsilon^{-1}k_*\Delta\left(\frac{z}{z_*}-1\right) = O(1), \tag{3.40}$$

hence to $\alpha = 1$ in (3.28) and thus $Z_{\rm II} = O(\epsilon^{1/3}) \ll 1$. For this range of Z, the integral in (3.26) is dominated by wavenumbers k in an $O(1)$ neighbourhood of the central wavenumber $\epsilon^{-1}k_*$, corresponding to $\beta = 1$ in (3.29). The associated regime, which we term Regime II$_{\rm B}$, is a limit Regime II, obtained when some terms are negligible (notably the first term in the phase function (3.37)). This makes it possible to derive an expression for w_1 simpler than (3.35)which we will subsequently use to compute the mean-flow forcing. This expression is derived in Appendix A.3 and given by

$$w_1 \doteq \frac{hfJ^{1/2}\left(1+\nu_*^2\right)^{1/4}\left((k_*\Delta)^2{\rm Ro}^2-1\right)^{1/4}}{(k_*\Delta)^{1/2}X}\,{\rm e}^{-\left(a^2/X^2-Z\right)^2/2}g(y), \tag{3.41}$$

where

$$a = \frac{J\sqrt{1+\nu_*^2}}{\sqrt{2}k_*\Delta} \tag{3.42}$$

and

$$X = (k_*\Delta)^{-3/2}\left(k_*x + J\left(\frac{k_*\sqrt{1+\nu_*^2}\Delta{\rm Ro}}{\sqrt{(k_*\Delta)^2{\rm Ro}^2-1}} + \frac{\nu_*^2}{\sqrt{1+\nu_*^2}}D_{\rm II}\right)\right). \tag{3.43}$$

According to this, the wavepacket is centred on the curve

$$X = X_{\rm c} = \left(\frac{J^2\left(1+\nu_*^2\right)}{(k_*\Delta)^2(Z+\sqrt{2+Z^2})}\right)^{1/2} \tag{3.44}$$

in the (X,Z)-plane (obtained by maximising (3.41)) and localized in a region of order-one size in both the X and Z direction. In view of (3.40) and (3.43), this corresponds to a region of streamwise extent $O((k_*\Delta)^{1/2}\Delta)$, thus much larger than the size Δ of the mountain, located an $O((k_*\Delta)^{1/2}\Delta)$ distance downstream of the topography, and of $O(\delta_*)$ vertical extent. Thus, the prediction of ray tracing of a wavepacket that diverges to infinity as the dominant inertial level is approached is replaced in Regime II$_{\rm B}$ (and hence in Regime II) by a large-but-finite horizontal shift.

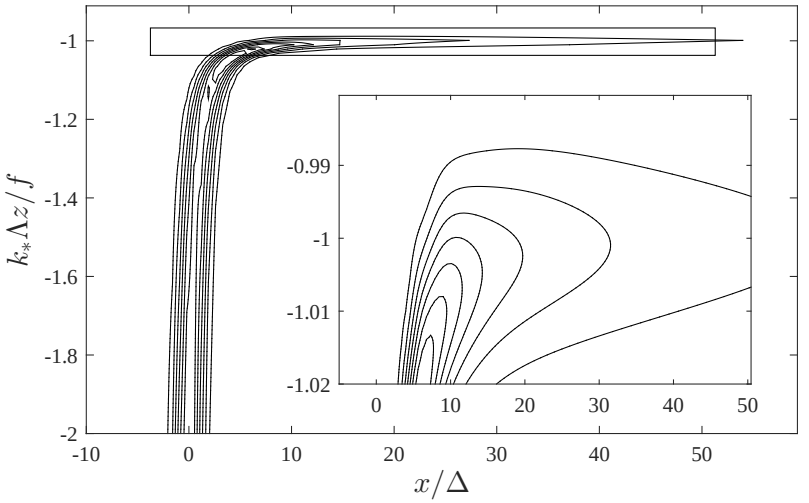

FIGURE 2. Vertical velocity amplitude $|w_1|$ in the (x, z) plane obtained by numerical integration of (3.21) for the parameters in (3.45) (7 equispaced contours with velocity in the range $[0.04, 0.28] \times Uhk_*/\sqrt{2\pi}$ are shown). The inset is a zoom on the rectangle region indicated in the main panel.

We remark that the three regimes identified by the saddle-point analysis can be interpreted physically. Regime I is the ray-tracing regime, which is unaffected by the singularities of the wave solution. Regime II is controlled by the singularity at the lower inertial level, and Regime IIB is its part dominated by inertial-level absorption.

3.3. *Numerical results*

In this section, we compare the asymptotic predictions for w_1 with direct numerical computations of the integral in (3.26). We first take the parameters

$$\mathrm{Ro} = 0.02, \quad k_*\Delta = 100, \quad l_*\Delta = 100, \quad J = 100 \quad \text{and} \quad \nu_* = 1, \tag{3.45}$$

so $\zeta_{\mathrm{b}*} = k_*\Delta\mathrm{Ro} = 2$. These are not particularly realistic but enable a comparison in conditions where the asymptotic assumptions hold unambiguously. Realistic parameters are considered at the end of the section. We concentrate on the amplitude $|w_1|$ in the (x, z) cross-section where it is maximum, since the structure in y is simply the Gaussian structure of the mountain envelope, albeit with a shift.

Figure 2 shows a contour plot of $|w_1|$ obtained numerically. Away from the dominant inertial level, $k_*\Lambda z/f = -1$, the wavepacket is only sightly deflected from the vertical. Closer to the dominant inertial level, the wavepacket shows a significant bend; we can read off from the inset that the peak of the wavepacket at the dominant inertial level is around $x/\Delta \approx 12$, in agreement with the peak value predicted in (3.43) which gives $X_{\mathrm{c}} = 2^{1/4}$. This figure is more a qualitative illustration than a quantitative comparison which we carry out next.

Figure 3 provides a detailed comparison of the numerical and asymptotic predictions for $|w_1|$. Its four panels show $|w_1|$ as a function of x/Δ at four different altitudes. Panel (a) corresponds to $-k_*\Lambda z/f = 1.5$, sufficiently far below the dominant inertial level for the Regime I asymptotics to be apply. As expected, the asymptotic predictions of Regime I (solid line) matches the numerical results (circles), with a wavepacket that takes the bell shape of the mountain enevelope, while the predictions of Regime II (dashed line) do not.

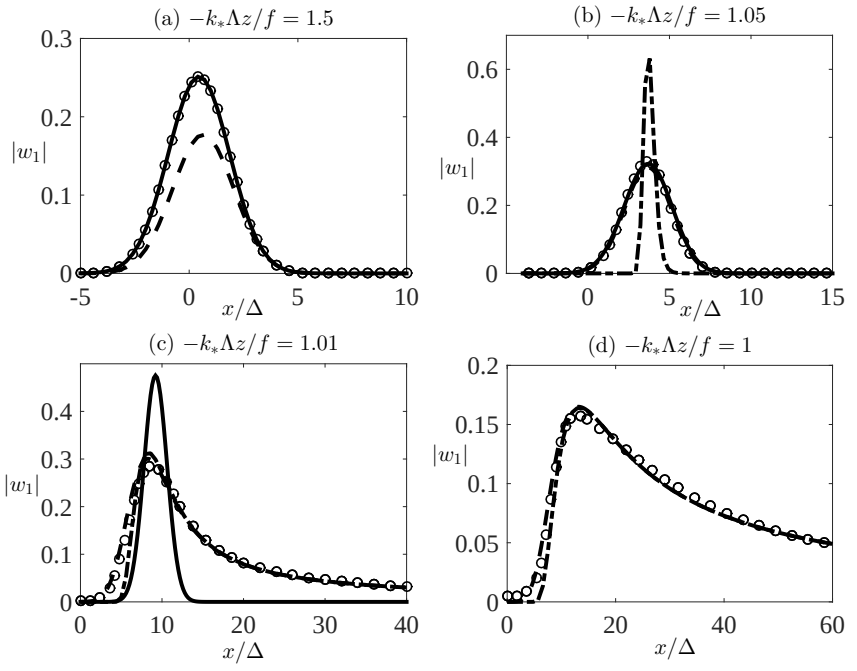

FIGURE 3. Vertical velocity amplitude $|w_1|$ normalized by $Uhk_*/\sqrt{2\pi}$ as a function of x/Δ for the altitudes given by $-k_*\Lambda z/f = 1.5$ (a), 1.05 (b), 1.01 (c) and 1 (d), and the parameters in (3.45). Numerical results (circles) are compared with the asymptotic predictions of Regime I (solid line, shown in panels (a)–(c)), Regime II (dashed line), and Regime $\mathrm{II_B}$ (dash-dotted line, shown in panels (b)–(d)).

Panel (b) shows the wavepacket closer to the dominant inertial level, for $-k_*\Lambda z/f = 1.05$, in a region where Regime I and Regime II overlap: the predictions of both regimes match the numerical results. The Regime $\mathrm{II_B}$ approximation is also shown (dash-dotted line) and, unsurprisingly, is found to be invalid. Closer still to the dominant inertial level, as shown in panel (c) for $-k_*\Lambda z/f = 1.01$, the Regime I approximation breaks down. The Regime II predictions match the numerical results closely, while those of Regime $\mathrm{II_B}$ are accurate for x large enough. As expected, the wavepacket is no longer bell shaped, and its peak is shifted by an $O((k_*\Delta)^{1/2}\Delta)$ amount to the right (since $x/\Delta \approx 10 = (k_*\Delta)^{1/2}$) in agreement with (3.43) and (3.44). Finally, at the dominant inertial level as shown in panel (d), the predictions of both Regime II and Regime $\mathrm{II_B}$ coincide and match the numerical results in most of range of x, except to the very left of the peak where Regime $\mathrm{II_B}$ underestimates the amplitude. As discussed above, the peak of the wavepacket remains at a finite $O((k_*\Delta)^{1/2}\Delta)$ position. Crucially for mean-flow forcing, the maximum amplitude is also strongly reduced as a result of absorption.

We now consider a more realistic parameter choice relevant to the atmosphere. Taking $N = 1.4\times10^{-2}\,\mathrm{s}^{-1}$, $f = 10^{-4}\,\mathrm{s}^{-1}$, $\Lambda = 1.4\times10^{-4}\,\mathrm{s}^{-1}$, $H = 5\,\mathrm{km}$, $\Delta = 3.5\times10^{2}\,\mathrm{km}$ and $k_* = 2.8\times10^{-4}\mathrm{m}^{-1}$ gives

$$\mathrm{Ro} = 0.4, \quad k_*\Delta = 5, \quad l_*\Delta = 5, \quad J = 5 \ \text{ and } \ \nu_* = 1, \tag{3.46}$$

so $\zeta_{\mathrm{b}*} = k_*\Delta\mathrm{Ro} = 2$. The results for the form of the wavepacket are shown in Fig. 4. The accuracy of the asymptotic approximations has degraded considerable compared with that in Fig. 4, unsurprisingly, perhaps, given that the error scales like $\mathrm{Ro}^{1/2} \approx$

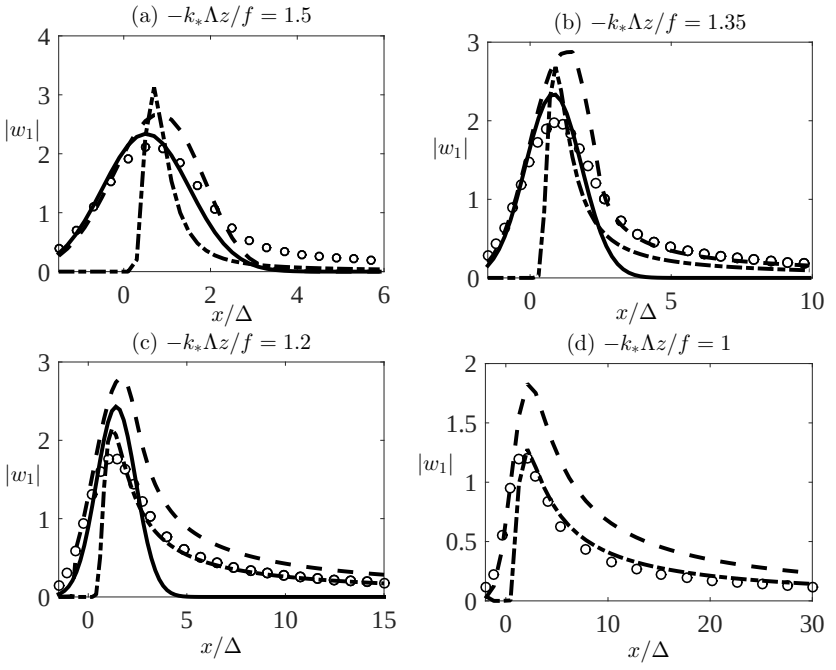

FIGURE 4. Same as Fig. 3 but for the parameters in (3.46) and for $-k_*\Lambda z/f = 1.5$ (a), 1.35 (b), 1.2 (c), 1 (d).

0.6. Nonetheless, there remains a reasonable qualitative match between asymptotic and numerical results which suggests our approximations remain useful.

4. Wave–mean-flow interaction

Section 3 shows that the wave amplitude changes suddenly across the inertial layer. In this section, we exploit our asymptotic expression for the wavepacket structure to derive the mean force exerted in this layer as a result of this change, and to calculate the mean-flow response. The important quantity for this force is the EP flux, which has long been recognized as the relevant diagnostic (Eliassen & Palm 1961; Andrews & McIntyre 1976; Boyd 1976; Edmon *et al.* 1980).

Two types of mean-flow response need to be distinguished: the far-field response, and the local response. The far-field response is the net change in the mean flow that persists far downstream of the mountain; it is a consequence of a change of the horizontally integrated EP flux due to absorption. In contrast, the local response is the mean-flow change caused by local EP flux changes without far-field impact because they integrate to zero horizontally. As discussed in §3, the net EP flux change is concentrated in the inertial layer where the Regime $\mathrm{II_B}$ approximation applies; below this, the waves are transient horizontally in space and leave no net mean-flow response, in agreement with non-acceleration results. In the remainder of this section, we derive the equation governing mean-flow response (§ 4.1), compute the EP flux divergence that appears as the sole forcing term in this equation (§ 4.2), and compute the mean-flow change asymptotically, taking advantage of the the thinness of the inertial layer (§ 4.3)

4.1. *Governing equation*

Taking advantage of the small Rossby number, the mean flow is calculated using quasi-geostrophic theory. By taking the horizontal curl of the horizontal momentum equation (2.2a), applying $\partial_z f/N^2$ to (2.2c) and using the incompressibility (2.2d), we obtain

$$\partial_t\left(v_x - u_y + \partial_z\left(\frac{f}{N^2}b\right)\right) + \underbrace{(\partial_{xx}-\partial_{yy})(uv) + \partial_{xy}(v^2-u^2)}_{\text{(a)}} + \underbrace{\partial_z\left(\frac{f}{N^2}\partial_z(wb)\right)}_{\text{(b)}}$$
$$+ \underbrace{\partial_{xz}\left(wv + \frac{f}{N^2}ub\right) - \partial_{yz}\left(wu - \frac{f}{N^2}vb\right)}_{\text{(c)}} = 0. \quad (4.1)$$

The waves and mean flow are separated by the small-scale average defined as

$$\langle\ \cdot\ \rangle = \frac{1}{D^2}\int_x^{x+D}\int_y^{y+D} \cdot\, \mathrm{d}\boldsymbol{x}', \quad (4.2)$$

where $k_*^{-1} \ll D \ll \Delta$. Because of their small spatial scale, the waves have zero average. Applying this average to (4.1), and using the smallness of the wave amplitude and Rossby number to retain the leading order terms for both wave and mean flow, we obtain

$$(\partial_t + \Lambda z\partial_x)\left(\nabla^\perp\cdot\boldsymbol{U} + \partial_z\left(\frac{f}{N^2}\langle b_2\rangle\right)\right) + \nabla^\perp\cdot\partial_z\boldsymbol{\mathcal{F}} = 0, \quad (4.3)$$

where $\nabla^\perp = (-\partial_y,\, \partial_x)$ denotes the horizontal curl, and

$$\boldsymbol{\mathcal{F}} = \left(\langle u_1 w_1\rangle - \frac{f}{N^2}\langle v_1 b_1\rangle,\, \langle v_1 w_1\rangle + \frac{f}{N^2}\langle u_1 b_1\rangle\right) \quad (4.4)$$

is the vertical part of the Eliassen–Palm (EP) flux Eliassen & Palm (1961). In (4.3), the mean flow is in geostrophic balance, with

$$\langle\boldsymbol{u}_2\rangle = (\boldsymbol{U}, 0) = (U, V, 0) = (-\partial_y\Psi,\, \partial_x\Psi, 0) \quad \text{and} \quad \langle b_2\rangle = f\partial_z\Psi, \quad (4.5)$$

where the streamfunction Ψ remains to be determined.

If there is no wave effect, $\boldsymbol{\mathcal{F}} = 0$, (4.3) reduces to the quasi-geostrophic potential-vorticity (QGPV) equation. Note that term (c) in (4.1) is the only quadratic wave term to contribute to (4.3): term (a) is $O(\delta_*/H)$ smaller than term (c) because of the vertically thinness of inertial layer; term (b) has zero average because w_1 and b_1 are out of phase in the limit of large J (see (3.12c)).

The boundary condition associated with (4.3) is obtained by taking the average of (2.3), retaining terms up to second order in the wave amplitude to find

$$\langle w_2\rangle = \langle \mathbf{u}_1\cdot\nabla h_\mathrm{t} - h_\mathrm{t}\partial_z w_1 - \Lambda h_\mathrm{t}\partial_x h_\mathrm{t}\rangle = \langle \mathbf{u}_1\cdot\nabla h_\mathrm{t} + h_\mathrm{t}\nabla\cdot\mathbf{u}_1 - \Lambda h_\mathrm{t}\partial_x h_\mathrm{t}\rangle$$
$$= \left\langle\nabla\cdot(\mathbf{u}_1 h_\mathrm{t}) - \Lambda\partial_x\left(h_\mathrm{t}^2/2\right)\right\rangle = 0, \quad (4.6)$$

where $\mathbf{u}_1 = (u_1,\, v_1)$, and the incompressibility condition (3.5d) is used.

One significant feature of the EP flux is its conservation when the background flow possesses certain symmetries, leading to the non-acceleration theorem (Charney & Drazin 1961): waves do not force the mean flow unless there exists a singularity or some dissipation. In our setup, the background shear flow has x- and y-symmetry, and EP flux conservation is easily demonstrated for a plane wave with wavevector $\boldsymbol{k} = (k, l)$: applying the polarization relation (3.12) to (4.4), we obtain the plane-wave expression of

the EP flux,

$$\boldsymbol{\mathcal{F}} = (F, \nu F), \quad \text{with} \quad F = \frac{-\Lambda}{f}\frac{1}{1+\nu^2}\mathrm{Re}\left(\mathrm{i}\frac{1-\zeta^2}{\zeta^2}\hat{w}_\zeta(\boldsymbol{k})\hat{w}^*(\boldsymbol{k}) - \nu\frac{\hat{w}(\boldsymbol{k})\hat{w}^*(\boldsymbol{k})}{\zeta^2}\right). \quad (4.7)$$

Its conservation is deduced from (3.9) by multiplication of $\hat{w}$ by its complex conjugate $\hat{w}^*$ and subtraction of the conjugate of the resulting equation to find

$$\partial_z F = 0. \quad (4.8)$$

This conservation does not hold across the inertial level singularities $\zeta = \pm 1$. Across the lower one, $\zeta = 1$, the plane wave EP flux attenuates to an exponentially small value, leading to the wave forcing of the mean flow in the inertial layer (Regime $\mathrm{II_B}$). We now compute the EP flux in this layer.

4.2. *Eliassen–Palm flux*

The derivation of the EP flux is greatly simplified by observing that, in the saddle-point approximations valid in Regimes I and II, the relations of the various wave fields u_1, v_1, etc. associated with the wavepacket to w_1 mirror the polarisation relations (3.12). This is because the rapid dependence in x of the wave solution corresponds to a plane wave with (possibly complex) wavenumber $\boldsymbol{k}_\mathrm{s}$ given by a saddle-point value of $\boldsymbol{k}$ (see Appendix A). Using the notation $\zeta_\mathrm{s} = -k_\mathrm{s}\Lambda z/f$, we obtain

$$u_1 = \frac{\mathrm{i}(\zeta_\mathrm{s} - \mathrm{i}\nu_*)}{K_\mathrm{s}\zeta_\mathrm{s}(1+\nu_*^2)}w_{1z} - \frac{\mathrm{i}\Lambda\nu_*^2}{f\zeta_\mathrm{s}(1+\nu_*^2)}w_1, \quad (4.9a)$$

$$v_1 = -\frac{1-\mathrm{i}\nu_*\zeta_\mathrm{s}}{K_\mathrm{s}\zeta_\mathrm{s}(1+\nu_*^2)}w_{1z} + \frac{\mathrm{i}\Lambda\nu_*}{f\zeta_\mathrm{s}(1+\nu_*^2)}w_1, \quad (4.9b)$$

$$b_1 = -\frac{\mathrm{i}\Lambda(1-\mathrm{i}\nu_*\zeta_\mathrm{s})}{K_\mathrm{s}\zeta_\mathrm{s}^2(1+\nu_*^2)}w_{1z} + \mathrm{i}\frac{\Lambda^2}{f}\left(\frac{\mathrm{i}\nu_*}{\zeta_\mathrm{s}^2(1+\nu_*^2)} + \frac{J^2}{\zeta_\mathrm{s}}\right)w_1, \quad (4.9c)$$

where we also have used that $\nu_\mathrm{s} = l_\mathrm{s}/k_\mathrm{s} \sim l_*/k_* = \nu_*$ to leading order. Correspondingly, a derivation that parallels that of (4.7) gives the x-component of the wavepacket EP flux as

$$F = \frac{1}{1+\nu_*^2}\mathrm{Re}\left(\frac{\mathrm{i}}{k_\mathrm{s}}\frac{1-\zeta_\mathrm{s}^2}{\zeta_\mathrm{s}^2}w_{1z}w_1^* - \nu_*\frac{w_1 w_1^*}{\zeta_\mathrm{s}^2}\right). \quad (4.10)$$

This can be simplified further. Focussing on Regime $\mathrm{II_B}$, we observe that the $O(\epsilon)$ vertical scale implies that the first term in the brackets in (4.10) dominates the second, that k_s can be approximated by k_*, and that ζ_s can be approximated by 1 except in the factor $1-\zeta_\mathrm{s}$ of $1-\zeta_\mathrm{s}^2$. This leads to the simple expression

$$F = \frac{2(1-\zeta_\mathrm{s})}{k_*(1+\nu_*^2)}\mathrm{Re}\,(\mathrm{i}w_{1z}w_1^*). \quad (4.11)$$

Now, using that $\partial_z = -k^*\Delta\Lambda\partial_Z/f$, we obtain from the form of w_1 in (A 15) that, to leading order,

$$w_{1z} \sim \frac{\mathrm{i}(k_*\delta)^{3/2}k_*\Lambda}{f}w_1. \quad (4.12)$$

Introducing this result into (4.11) and using that

$$\zeta_\mathrm{s} = 1 + \frac{1}{k_*\Delta}(K_\mathrm{s} + Z), \quad (4.13)$$

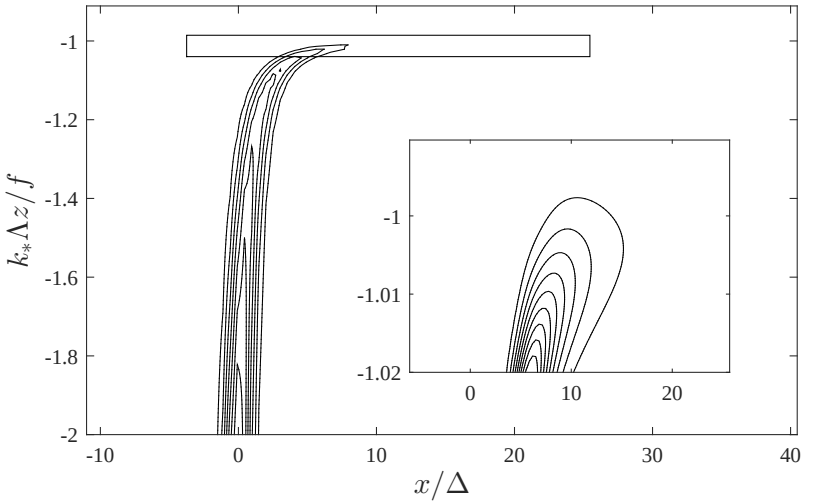

FIGURE 5. Contours of the EP flux in (4.15) normalized by the largest value at the bottom $(3/4)^{3/4}\mathrm{e}^{-3/4}E$ for the parameters in (3.45); 7 equispaced contours in the range $[0.125, 0.875]$ are shown. The contours can be compared with those of the vertical velocity $|w_1|$ shown in Fig. 2: although the two fields obey the same scaling, the maximum of the EP flux is closer to the mountain. The inset zooms on the rectangular box indicated in the main panel.

421 together with the explicit form (A 14) of K_s, we find that

$$F = \frac{J^2\Lambda}{(k_*\Delta)^{3/2}fX}|w_1|^2. \tag{4.14}$$

422 The explicit form of w_1 in (3.41) can finally be used to obtain the explicit expression

$$F = \frac{E}{X^3}\,\mathrm{e}^{-\left(a^2/X^2-Z\right)^2} g^2(y), \tag{4.15}$$

423 where

$$E = \frac{J^3\Lambda h^2 f\left((k_*\Delta)^2\mathrm{Ro}^2-1\right)^{1/2}\left(1+\nu_*^2\right)^{1/2}}{(k_*\Delta)^{5/2}} \tag{4.16}$$

424 is a constant controlling the amplitude of F. This expression only holds for $X > 0$; for
425 $X < 0$, the EP flux is exponentially small. We emphasise the remarkably simple form
426 of (4.15): notwithstanding the many parameters involved, the formula is well suited for
427 practical use in parameterisations.

428 We illustrate the form of the EP flux in Fig. 5 by showing its contours in the (x, z) cross-
429 section where it is maximised, using the parameters in (3.45). The EP flux is computed
430 from the WKB linear solution (3.19) and polarization relation (3.12). The validity of the
431 asymptotic approximation is confirmed by Fig. 6 which compares the EP flux obtained
432 numerically with the asymptotic approximation at the dominant inertial level.

433 By integrating (4.15) over x and y, we obtain the horizontally integrated EP flux

$$\overline{F} = \frac{\pi J\Delta^2\Lambda h^2 f\left((k_*\Delta)^2\mathrm{Ro}^2-1\right)^{1/2}}{2\left(1+\nu_*^2\right)^{1/2}}(1+\mathrm{erf}Z), \tag{4.17}$$

434 where the decay of the error function to 0 as $Z \to -\infty$ (above the inertial layer) clearly
435 captures wave absorption. As $Z \to \infty$, i.e., well below the dominant inertial level, $\overline{F}$

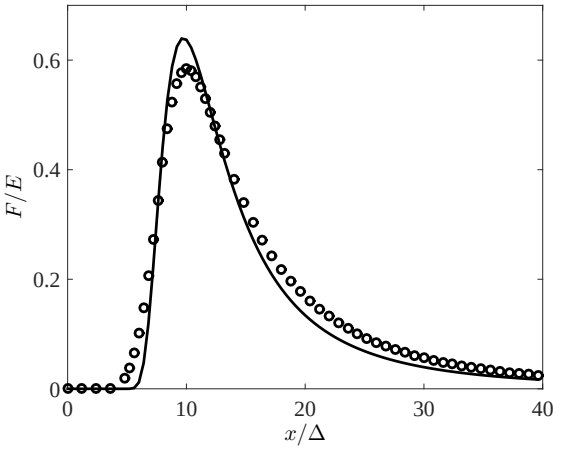

FIGURE 6. EP flux at the dominant inertial level for the parameters in (3.45): numerical results (circles) are compared with the prediction of the Regime $\mathrm{II_B}$ approximation (solid line).

tends to the constant value

$$\overline{F}_{\rm tot} = \frac{\pi J \Delta^2 \Lambda h^2 f \left((k_*\Delta)^2 \mathrm{Ro}^2 - 1\right)^{1/2}}{(1+\nu_*^2)^{1/2}}. \tag{4.18}$$

This matches the horizontally integrated EP flux at the ground, since the flux is conserved below the inertial layer. We check this in Appendix B. We note that $\overline{F}_{\rm tot}$ is finite in the limit $f \to 0$ where it is given by $\overline{F}_{\rm tot} = \pi N \Lambda \Delta^2 h^2 k_* H$. From (4.17), we can also estimate the wave drag per unit area, defined as the vertical derivative of horizontally integrated EP flux divided by Δ^2:

$$\overline{f(Z)} = \frac{\partial_z \overline{F(Z)}}{\Delta^2} = -\frac{\sqrt{\pi}}{2} \Lambda N \Delta h^2 k_*^2 \frac{k_*}{|\boldsymbol{k_*}|} ((k_*\Delta)^2 \mathrm{Ro}^2 - 1)^{1/2} \mathrm{e}^{-Z^2}, \tag{4.19}$$

where $|\boldsymbol{k_*}| = \sqrt{k_*^2 + l_*^2}$ is the amplitude of dominant wavenumber.

4.3. *Mean-flow response*

We now consider the mean-flow response to the wave drag associated with the z-dependent EP flux (4.15). We compute the steady flow response by solving the QGPV equation (4.3) asymptotically, taking advantage of the thinness of the inertial layer where the wave drag acts to apply matched asymptotics. Thus the domain $z > -H$ is separated into an inner region around the inertial level $z \approx z_*$, specifically $Z = -k_*^2 \Delta \Lambda (z - z_*)/f = O(1)$, and an outer region where the wave drag is absent. Simplifications arise because the spatial scale in the x-direction is longer than in the y-direction; this is made explicit using the variable X defined in (A 16), with $X = O(1)$ implying that $x = \Delta \times O((k_*\Delta)^{1/2})$

We denote the streamfunction associated with the wave-induced mean flow in the inner and outer regions by $\Psi(X, y, Z)$ and $\psi(X, y, z)$, respectively. In the inner region, considering the scalings of Regime $\mathrm{II_B}$, the steady ($\partial_t = 0$) QGPV equation (4.3) becomes

$$\epsilon^{1/2} k_* (k_*\Delta)^{-3/2} (U_* \partial_X + \nabla^\perp \Psi \cdot \nabla) \left(\epsilon k_*^2 (k_*\Delta)^{-3} \partial_{XX} \Psi + \partial_{yy} \Psi + \frac{k_*^4 \Delta^2}{\epsilon^2 J^2} \partial_{ZZ} \Psi \right)$$
$$= \frac{k_*^2 \Lambda \Delta}{\epsilon^2 f} \partial_{yZ} F, \tag{4.20}$$

where ∇ and $\nabla^\perp$ are gradients with respect to the scaled variables (X, y), $U_* = -\Lambda z_* = f/k_*$ is the background velocity at the dominant inertial level, and we have included the bookkeeping parameter ϵ. On the right-hand side we have neglected the x derivative of $\partial_z F$ against the y-derivative, owing to the asymptotically larger scales in x.

For sufficiently small mountain height, Eq. (4.20) can be linearised; we make explicit below the condition for this approximation to hold. Retaining only the leading-order terms in (4.20) reduces this to

$$\frac{k_*^3(k_*\Delta)^{1/2}}{\epsilon^{3/2}J^2}U_*\partial_{XZZ}\Psi = \frac{k_*^2\Lambda\Delta}{\epsilon^2 f}\partial_{yZ}F. \tag{4.21}$$

Since F is exponentially small for $X < 0$, we can integrate (4.21) for $X > 0$ to obtain

$$\partial_{ZZ}\Psi = Q, \tag{4.22}$$

where

$$Q = Q(X, y, Z) = \frac{J^2\Lambda(k_*\Delta)^{1/2}}{\epsilon^{1/2}U_*k_*^2 f}\int_0^X \partial_{yZ}F(X', y, Z)\,\mathrm{d}X' \tag{4.23}$$

can be interpreted as a scaled wave-induced PV. This can be computed explicitly using (4.15) to find

$$Q = \frac{J^3\Lambda^2\Delta h^2((k_*\Delta)^2\mathrm{Ro}^2 - 1)^{1/2}}{f(k_*\Delta)(1+\nu_*^2)^{1/2}}\,\mathrm{e}^{-(a^2/X^2 - Z)^2}\partial_y g^2. \tag{4.24}$$

Eq. (4.22) is readily integrated, leading to

$$\Psi(X, y, Z) = \int_0^Z\int_0^{Z'} Q(x, Y, Z'')\,\mathrm{d}Z'\mathrm{d}Z'' + C_1(X, y)Z + \epsilon^{-1}C_2(X, y), \tag{4.25}$$

where C_1 and C_2 are integration 'constants' that are determined by matching the outer solution. We have anticipated that the Z-independent term is an order ϵ^{-1} larger than the other terms. Matching requires the asymptotic behaviour of Ψ as $Z \to \pm\infty$, found to be

$$\begin{aligned}\Psi(X, y, Z) \sim & Z\left(\int_0^{\pm\infty} Q(X, y, Z')\,\mathrm{d}Z' + C_1(X, y)\right) + \epsilon^{-1}C_2(X, y)\\ & - \int_0^{\pm\infty} Z'Q(X, y, Z')\,\mathrm{d}Z'\end{aligned} \tag{4.26}$$

as $Z \to \pm\infty$.

In the outer region, the QGPV equation (4.3) is

$$\Lambda z\partial_X\left(\partial_{yy}\psi + \epsilon k_*^2(k_*\Delta)^{-3}\partial_{XX}\psi + \frac{f^2}{N^2}\partial_{zz}\psi\right) = 0, \tag{4.27}$$

which, to the leading order, reduces to

$$\Lambda z\partial_X(\partial_{yy}\psi + \frac{f^2}{N^2}\partial_{zz}\psi) = 0. \tag{4.28}$$

Integrating in X, we find that

$$\partial_{yy}\psi + \frac{f^2}{N^2}\partial_{zz}\psi = 0. \tag{4.29}$$

This is best solved using a Fourier transform in the y direction. Denoting this transform

by a hat, we have

$$\hat{\psi} = \begin{cases} \epsilon^{-1}\hat{C}_3(X,l)\mathrm{e}^{-N|l|(z-z_*)/f} & \text{for } z > z_* \\ \epsilon^{-1}\hat{C}_4(X,l)\mathrm{e}^{-N|l|(z-z_*)/f} + \epsilon^{-1}\hat{C}_5(X,l)\mathrm{e}^{N|l|(z-z_*)/f} & \text{for } z < z_* \end{cases}, \tag{4.30}$$

applying a vanishing boundary condition as $z \to \infty$. Combining the condition (4.6) of zero mean vertical velocity with the buoyancy equation $U\partial_X\psi_z = 0$ stemming from (2.2c), we find the condition $\psi_z = 0$ at the lower boundary $z = -H$. This implies

$$\hat{C}_4\mathrm{e}^{N|l|(H+z_*)/f} = \hat{C}_5\mathrm{e}^{-N|l|(H+z_*)/f}. \tag{4.31}$$

We now match (4.30) to (4.26) to determine $\hat{C}_3$, $\hat{C}_4$ and $\hat{C}_5$, and hence the outer solution, completely. Substituting $z - z_* = -\epsilon f Z/(k_*^2\Delta\Lambda)$ into (4.30), expanding in powers of ϵ and matching with (4.26), we find that

$$\hat{C}_4 + \hat{C}_5 = \hat{C}_3\,(= \hat{C}_2), \tag{4.32}$$

and

$$\begin{aligned} \hat{C}_4 - \hat{C}_5 - \hat{C}_3 &= \frac{k_*^2\Delta}{J|l|}\int_{-\infty}^{\infty}\hat{Q}(X,l,Z')\,\mathrm{d}Z' \\ &= \frac{\sqrt{\pi}J^2(k_*\Delta)\Lambda^2h^2((k_*\Delta)^2\mathrm{Ro}^2-1)^{1/2}}{f(1+\nu_*^2)^{1/2}}\frac{\widehat{\partial_y g^2}}{|l|}. \end{aligned} \tag{4.33}$$

Thus, (4.31), (4.32) and (4.33) provides three equations for $\hat{C}_3$, $\hat{C}_4$ and $\hat{C}_5$ and hence determine the mean flow.

Remarkably, the right-hand side of (4.33) does not depend on X. As a result, ψ, Ψ and thus the entire mean-flow response does not change downstream of the mountain. Our solution suggests that there is a jump in this response, from a zero value for $X < 0$ to the X-independent value for $X > 0$. This is an artefact of the asymptotic approximation: the transition to a non-zero mean flow is in fact smooth. Its detailed form could be obtained using the approximation of the wave fields in Regime II. Here we only note that the scaling of Regime II indicates that the transition region has a characteristic length $x/\Delta = O((k_*\Delta)^{1/3})$, asymptotically smaller than the $O((k_*\Delta)^{1/2})$ scale that is resolved by the Regime IIB approximation used in our computation of the mean-flow response, hence the apparent discontinuity.

Eq. (4.33) provides an estimate for the order of magnitude of the mean-flow response. Recalling that the change in mean velocity is $-\partial_y\psi$ with the y-scale Δ, and noting that the maximum value of ψ is $O(\hat{C}_3)$, we estimate the wave-induced mean velocity as

$$U_\mathrm{w} = O\left(J^2(k_*\Delta)\mathrm{Ro}\left(\frac{h}{H}\right)^2 U_\mathrm{b}\right). \tag{4.34}$$

Since $(k_*\Delta)\mathrm{Ro} = O(1)$, this indicates that $U_\mathrm{w} \ll U_\mathrm{b}$, as required for the linearisation of the QGPV equation, provided that $J(h/H) \ll 1$.

To illustrate our results, we have calculated the mean-flow response for $J = k_*\Delta$, $l_* = 0$ and $\zeta_{\mathrm{b}*} = 2$. The linear system (4.31), (4.32) and (4.33) is readily solved for $\hat{C}_3$, $\hat{C}_4$ and $\hat{C}_5$, leading to $\hat{\psi}$ and, after Fourier inversion, to the mean flow $\langle u_2\rangle = -\partial_y\psi$. This is displayed in Fig. 7. Observe that the mean-flow response to the wave drag localised in the thin inertial layer is distributed through the entire depth of the fluid, and that the total mean-flow change $\int\langle u_2\rangle\,\mathrm{d}y$ vanishes at each altitude since the streamfunction ψ vanishes as $y \to \pm\infty$.

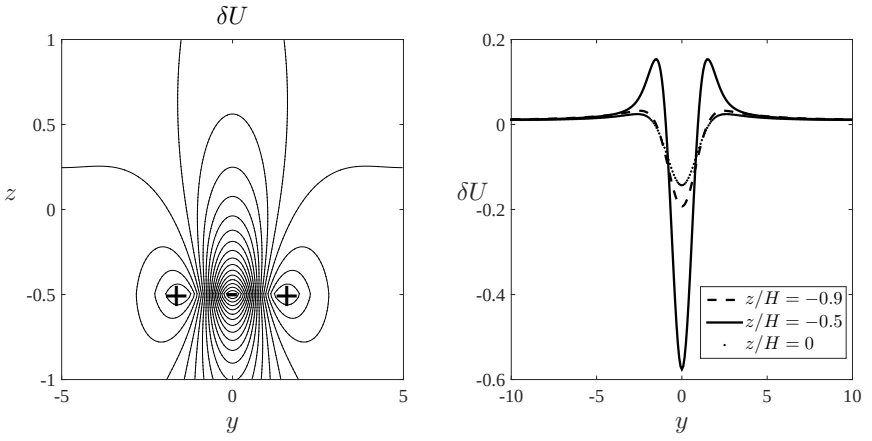

FIGURE 7. Mean-flow response. Left: contours of the wave-induced mean flow $\langle u_2 \rangle$, with the sign is indicated by $\pm$; 20 equispaced contours in the range $[-0.52, 0.13]$ are shown. Right: $\langle u_2 \rangle$ at $z/H = -0.9$, -0.5, 0, with $z = -0.5$ corresponding to the dominant inertial level. The mean flow is normalized by $\sqrt{3\pi} k_* J^2 \Lambda^2 h^2 / f$.

5. Conclusion

In this paper, we study the propagation of a mountain IGW wavepacket in a rotating shear flow and the mean flow generated as a result of wave absorption at inertial-level singularities. The broad wavenumber spectrum of the wavepacket and the dependence of the inertial-level altitude on wavenumber lead to a smearing-out of the singularities over a finite-thickness inertial layer where the mean-flow forcing concentrates. Thus, in contrast with the situation when rotation is neglected, dissipative processes can be neglected completely (except in brunch choosing across singularities) in the computation of the wavepacket and mean-flow response.

By applying a steepest descent method, we obtain explicit approximations for the form of the wavepacket in different regions characterised by their distance to the dominant inertial level, that is, the inertial level corresponding to the central wavenumber of the mountain profile. Our main conclusions concern the scaling of the wave solution and mean-flow forcing; they are indicated in Fig. 8. In Regime I, the wavepacket is sufficiently far away from the dominant inertial level that singular effects are not important. Standard ray-tracing results apply: the wavepacket resembles the topography, with envelope scale Δ. In Regime II the wavepacket is close to the dominant inertial level and hence strongly affected by the inertial-level singularity in the vertical structure (3.22) corresponding to a single wavenumber. As a consequence, ray tracing does not apply, and the wavepacket has a characteristic streamwise scale $(k_*\Delta)^{1/3}\Delta$, much longer than the scale of the topography. In Regime $\mathrm{II_B}$, a subregime of Regime II, the wavepacket is closer still to the dominant inertial level and is absorbed. We pay special attention to this regime since it is relevant to the region where the horizontally-integrated EP flux varies vertically, leading to a drag on the mean flow. Qualitatively, our most important conclusion is about the location of this region, found to be an $O((k_*\Delta)^{1/2}\Delta)$ distance downstream of the mountain and to have an $O((k_*\Delta)^{1/2}\Delta)$ horizontal extent. Since $k_*\Delta \gg 1$, this makes it evident that mountain waves exert their drag far downstream of the mountain. This is in sharp contrast with their parameterisations in atmospheric models which are typically columnar, assuming that wave propagation is purely vertical and imposing their wave drag right above the wave source (see Hasha *et al.* 2008, however).

Using the form of the wave solution in Regime $\mathrm{II_B}$, we compute the far-field mean-

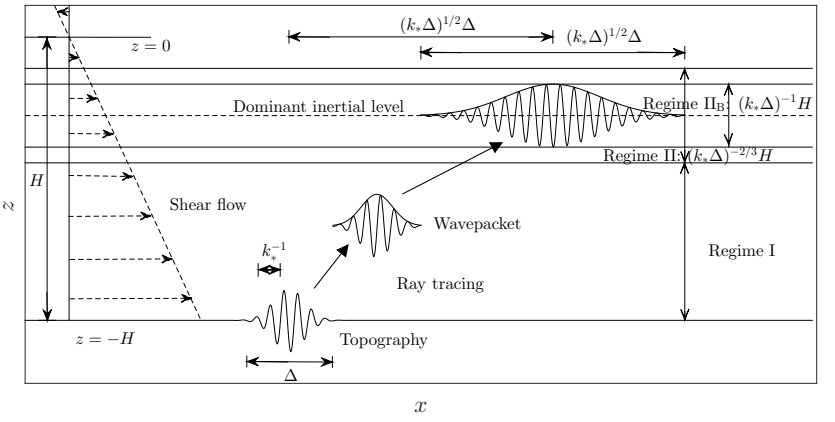

FIGURE 8. Scaling regimes for the mountain wavepacket: the wavepacket is generated by a backsheared flow over a two-scale topography, with a scale separation characterised by $k_*\Delta \ll 1$. Two distinguished regimes are found: Regime I and Regime II corresponding to distances from the dominant inertial level that are $O(H)$ and $O((k_*\Delta)^{-2/3}H)$, respectively. The wave drag is localised in a region described by the limiting Regime II$_B$, of thickness of $O(k_*\Delta H)$ around the dominant inertial level. This region is located a large, $O((k_*\Delta)^{1/2}\Delta)$ distance downstream of the mountain and extending horizontally over an $O((k_*\Delta)^{1/2}\Delta)$ scale.

flow response, taking advantage of the smallness of the Rossby number to use a quasi-geostrophic approximation. The vertical divergence of the EP flux, which controls the mean-flow response in this approximation, is localised in the thin inertial layer, with vertical scale $H/(k_*\Delta)$. The mean-flow response itself, however, has a large scale in both the horizontal and vertical directions because of the non-locality in the diagnostic relation between the mean potential vorticity and mean streamfunction in the quasi-geostrophic approximation.

An interesting feature of the mean-flow generation predicted by the Regime II$_B$ approximation is that it is zero in the region with $X = k_*^{-1/2}\Delta^{-3/2}x < 0$ but jumps to an X-independent value for $X \geqslant 0$. Implicit to this prediction is an assumption that $X = O(1)$, which gives the characteristic horizontal scale of the wavepacket in the inertial layer. The mean flow is in fact smoothly switched on over a shorter characteristic scale, specifically, $x/\Delta = O((k_*\Delta)^{1/3})$. This result can be obtained using the Regime II approximations, but we do not carry out detailed calculations which are complicated by the presence of a branch cut in (3.35).

We emphasise that our results are more general than might seem at first glance. Our derivations are based on the distinguished scaling $\mathrm{Ro} = O((k_*\Delta)^{-1})$, $J = O(k_*\Delta)$, with $k_*\Delta \gg 1$, and $Jh/H \ll 1$. In fact, their validity only requires that

$$J\frac{h}{H} \ll 1, \quad k_*\Delta \gg 1, \quad J \gg 1, \quad \mathrm{Ro} \ll 1 \quad \text{and} \quad \frac{k_*\Delta H}{f} > 1, \tag{5.1}$$

corresponding to the validity of the hypotheses of (i) linear wave, (ii) scale separation of the mountain height, (iii) WKB scaling as in Lott *et al.* (2012), (iv) quasi-geostrophic mean flow, and (v) the dominant inertial level located above ground, ensuring that the argument of the square root in (4.19) is positive. If the conditions in (5.1) are satisfied but the scaling differs from the assumed distinguished scaling, e.g. because $J \gg k_*\Delta$,

our results continue to hold and could in fact be simplified by taking into account the existence of additional small parameters, such as $\Delta k_*/J$ in our example.

We conclude by assessing the validity of the assumption of infinitesimally small viscosity, which leads to a vertical scale of wave absorption given by the inertial-layer thickness (3.14). For a finite viscosity, the viscous vertical scale $\delta_\mathrm{d} = (\nu N^2/k_*)^{1/3}/\Lambda$ is found by considering the Taylor–Goldstein equation with dissipation, $D_t^2\nabla^2 w + N^2 w_{xx} = \nu D_t \nabla^4 w$, with $D_t = \Lambda z \partial_x$. The ratio $\delta_\mathrm{d}/\delta_*$ which measures the relative strength of viscosity and rotation in setting up the wave vertical scale is then found as $\delta_\mathrm{d}/\delta_* = \Delta k_*^{5/3}(\nu N^2)^{1/3}/f$, independent of the shear Λ and relatively insensitive to the value of ν. Taking the atmospheric values $\nu = 10^{-8}\,\mathrm{m^2 s^{-1}}$, $N = 10^{-2}\,\mathrm{s^{-1}}$, $f = 10^{-4}\,\mathrm{s^{-1}}$, $k = 10^{-3}\,\mathrm{m^{-1}}$ and $\Delta = 10^4\,\mathrm{m}$ as an illustration, we compute $\delta_\mathrm{d}/\delta_* = 10^{-1}$, indicating a dominance of the rotation effects considered in this paper.

Acknowledgements. This research is funded by the UK Natural Environment Research Council (grant NE/J022012/1). J.-H. X. acknowledges financial support from the Centre for Numerical Algorithms and Intelligent Software (NAIS).

Appendix A. Details of wave solution

In this Appendix we provide details of the derivation of the saddle-point approximations to the wavepacket in §3.

A.1. *Regime I*

In this section we consider altitudes well below the inertial level, corresponding to the scaling (3.28) for z with $\alpha = 0$, that is, to

$$\zeta_* = -\frac{k_*\Lambda z}{f} = 1 + Z_\mathrm{I}, \quad \text{with} \quad Z_\mathrm{I} = O(1). \tag{A 1}$$

As discussed in §3.2, the associated distinguished regime is obtained by considering the scaling (3.29) for the wavenumber k. Substituting (3.29) and (A 1) into (3.26), we obtain

$$w_1 = \frac{\mathrm{i}U_\mathrm{b}hk_*\Delta}{\epsilon\sqrt{2\pi}}\frac{k_*}{\epsilon}\left(\frac{\epsilon}{k_*\Delta}\right)^\beta \mathrm{e}^{-\left(y - J\nu_* k_*^{-1}(1+\nu_*^2)^{-1/2}D_\mathrm{I}\right)^2/(2\Delta^2)} \tag{A 2}$$
$$\times \int_{-\infty}^{\infty} \frac{(1+Z_\mathrm{I})}{k_*\Delta\mathrm{Ro}}\left(\frac{(k_*\Delta)^2\mathrm{Ro}^2 - 1}{2Z_\mathrm{I} + Z_\mathrm{I}^2}\right)^{1/4} \mathrm{e}^{-\epsilon^{2\beta-2}(k_*\Delta)^{2-2\beta}K_\mathrm{I}^2/2 + \mathrm{i}\epsilon^{\beta-1}k_*(k_*\Delta)^{-\beta}K(x-X_\mathrm{cI})}\,\mathrm{d}K_\mathrm{I},$$

where

$$X_\mathrm{cI} = \frac{J}{k_*}\left(\sqrt{1+\nu_*^2}\left(\frac{1+Z_\mathrm{I}}{\sqrt{2Z_\mathrm{I}+Z_\mathrm{I}^2}} - \frac{k_*\Delta\mathrm{Ro}}{\sqrt{(k_*\Delta)^2\mathrm{Ro}^2 - 1}}\right) - \frac{\nu_*^2}{\sqrt{1+\nu_*^2}}D_\mathrm{I}\right) \tag{A 3}$$

with $D_\mathrm{I} = \ln(1 + Z_\mathrm{I} + (2Z_\mathrm{I} + Z_\mathrm{I}^2)^{1/2}) - \ln(\zeta_{\mathrm{b}*} + (\zeta_{\mathrm{b}*}^2 - 1)^{1/2})$. The expansion of $D(\zeta)$ results in the term $\mathrm{i}\epsilon^{\beta-1}k_*(k_*\Delta)^{-\beta}K(x - X_\mathrm{cI})$ in the exponential, in agreement with the scaling of $D(\zeta)$ in (3.31).

A distinguished regime is obtained by balancing the arguments of the exponential in (A 2), corresponding to the choice $\beta = 1$. With this, (A 2) can be integrated directly to find

$$w_1 \doteq hf(1+Z_\mathrm{I})\left(\frac{(k_*\Delta)^2\mathrm{Ro}^2 - 1}{2Z_\mathrm{I} + Z_\mathrm{I}^2}\right)^{1/4} \mathrm{e}^{-\left(y - J\nu_* k_*^{-1}(1+\nu_*^2)^{-1/2}D_\mathrm{I}\right)^2/(2\Delta^2)}\mathrm{e}^{-(x-X_\mathrm{cI})^2/(2\Delta^2)}, \tag{A 4}$$

ignoring the phase factor for simplicity.

A.2. *Regime II*

We now consider the wavepacket asymptotically close to the dominant inertial level, that is, for $\alpha > 0$ in the scaling (3.28) for z. In this case, the form of the expansion of $D(\zeta)$ in (3.32) depends on the smaller of α and β; therefore, a distinguished regime is naturally achieved with $\beta = \alpha$, leaving just the value of α to be determined. With $\alpha = \beta$, $D(\zeta)$ expands as

$$D(\zeta) \sim \left(\frac{\epsilon}{k_*\Delta}\right)^{\alpha/2} \sqrt{2(K_{\rm II}+Z_{\rm II})} - \ln(\zeta_{\rm b} + \sqrt{\zeta_{\rm b}^2-1}) - \left(\frac{\epsilon}{k_*\Delta}\right)^{\alpha} \frac{k_*\Delta {\rm Ro}}{\sqrt{(k_*\Delta)^2{\rm Ro}^2-1}} K_{\rm II}. \tag{A 5}$$

Substituting this and the expansions (3.28) and (3.29) for z and k into (3.26) leads to

$$\begin{aligned} w_1 = {} & \frac{{\rm i}U_{\rm b}hk_*^2\Delta}{2^{1/4}\epsilon^2\sqrt{2\pi}} \left(\frac{\epsilon}{k_*\Delta}\right)^{\alpha-1/4} \frac{(\zeta_{\rm b}^2-1)^{1/4}}{\zeta_{\rm b}} {\rm e}^{-\left(y - J\nu_* k_*^{-1}(1+\nu_*^2)^{-1/2} D_{\rm II}\right)^2/(2\Delta^2)} \\ & \times \int_{-Z_{\rm II}}^{\infty} \frac{1}{(K_{\rm II}+Z_{\rm II})^{1/4}} {\rm e}^{-\epsilon^{2\alpha-2}(k_*\Delta)^{2-2\alpha}K_{\rm I}^2/2} {\rm e}^{-{\rm i}\epsilon^{\alpha/2-1}(k_*\Delta)^{-\alpha/2}J(1+\nu_*^2)^{1/2}(2(K_{\rm II}+Z_{\rm II}))^{1/2}} \\ & \times {\rm e}^{{\rm i}\epsilon^{\alpha-1}K_{\rm II}\left(k_*(k_*\Delta)^{-\alpha}x + J(k_*\Delta)^{-\alpha}\left((1+\nu_*^2)^{1/2}k_*\Delta{\rm Ro}\left((k_*\Delta)^2{\rm Ro}^2-1\right)^{1/2} + \nu_*^2(1+\nu_*^2)^{-1/2}D_{\rm II}\right)\right)} {\rm d}K_{\rm II}, \end{aligned} \tag{A 6}$$

where $D_{\rm II} = -\ln(\zeta_{\rm b*} + \sqrt{\zeta_{\rm b*}^2-1})$. A distinguished regime is obtained by balancing the arguments of the first two exponentials, leading to $\alpha = 2/3$. The third exponential contributes to the same order as the other two when x is suitably rescaled. Substituting $\alpha = 2/3$ into (A 6) we obtain

$$\begin{aligned} w_1 \doteq {} & \frac{{\rm i}U_{\rm b}hk_*^2\Delta}{2^{1/4}\sqrt{2\pi}\epsilon^{19/12}(k_*\Delta)^{5/12}} g(y) \\ & \times \int_{-\infty}^{\infty} \frac{1}{(K_{\rm II}+Z_{\rm II})^{1/4}} {\rm e}^{\epsilon^{-2/3}(k_*\Delta)^{2/3}\left(-K_{\rm II}^2/2 - {\rm i}J(k_*\Delta)^{-1/3}\sqrt{1+\nu_*^2}\sqrt{2(K_{\rm II}+Z_{\rm II})} + {\rm i}K_{\rm II}X_{\rm II}\right)} {\rm d}K_{\rm II}, \end{aligned} \tag{A 7}$$

where $g(y)$ is the Gaussian given in (3.36). Here,

$$X_{\rm II} = \epsilon^{1/3}\left(k_*(k_*\Delta)^{-4/3}x + J(k_*\Delta)^{-4/3}\left(\sqrt{1+\nu_*^2}\frac{k_*\Delta{\rm Ro}}{\sqrt{(k_*\Delta)^2{\rm Ro}^2-1}} + \frac{\nu_*^2}{\sqrt{1+\nu_*^2}}D_{\rm II}\right)\right) \tag{A 8}$$

is assumed to be $O(1)$, thus indicating that the horizontal scale of the wavepacket in Regime II is larger by a factor $O(k_*\Delta)^{1/3}$ than its scale Δ in Regime I.

We can now apply the saddle point method to approximate (A 7) as

$$w_1 = \frac{{\rm i}U_{\rm b}hk_*^2\Delta}{2^{1/4}\epsilon^{5/4}(k_*\Delta)^{3/4}} q(K_{\rm IIs}) \sqrt{\frac{1}{p''(K_{\rm IIs})}} g(y) {\rm e}^{(k_*\Delta)^{2/3}P(K_{\rm IIs})}, \tag{A 9}$$

where

$$\begin{aligned} q(K_{\rm II}) &= \frac{1}{(K_{\rm II}+Z_{\rm II})^{1/4}}, \\ p(K_{\rm II}) &= -\frac{K_{\rm II}^2}{2} - {\rm i}J(k_*\Delta)^{-1/3}\sqrt{1+\nu_*^2}\sqrt{2(K_{\rm II}+Z_{\rm II})} + {\rm i}K_{\rm II}X_{\rm II}, \end{aligned} \tag{A 10}$$

and K_{IIs} is the saddle point such that $p'(K_{\mathrm{IIs}}) = 0$, with the prime denoting the derivative. The expression of p indicates that there are three saddle points, but only one is accessible by a steepest descent path that connects $-\infty$ to ∞. Note that the asymptotics of (3.35) for large Z_{II} matches the asymptotics of (A 2) for small Z_{I}. This confirms that there is no distinguished regime between Regimes I and II. The matching is also observed in Fig. 3(c).

A.3. *Regime II$_B$*

The previous two sections examined the two distinguished regimes of wave propagation. Here, we concentrate on the behaviour of the solution in the inertial layer of characteristic thickness δ_* as estimated in (3.14). This defines Regime II$_{\mathrm{B}}$, a subregime of Regime II characterised by $\alpha = 1$ and thus

$$\zeta_* = 1 + \left(\frac{\epsilon}{k_*\Delta}\right) Z, \tag{A 11}$$

with $Z = O(1)$. An argument analogous to that used for Regime II in §A.2 then shows that the wavenumber should be scaled as

$$k = \epsilon^{-1} k_* \left(1 + \frac{\epsilon}{k_*\Delta} K\right), \tag{A 12}$$

with $K = O(1)$. In principle we can deduce the form of w_1 in this regime from the Regime-II result (3.35). However, it is simpler and more illuminating to work out this form directly from the definition of w_1.

Introducing the scalings (A 11)–(A 12) into (3.26), we obtain

$$\begin{aligned} w_1 = {} & \frac{\mathrm{i}U_{\mathrm{b}} h k_* (k_*\Delta)^{1/4}}{2^{3/4}\pi^{1/2}\epsilon^{5/4}} g(y) \\ & \times \int_{-\infty}^{\infty} \frac{\mathrm{e}^{-\frac{K^2}{2}}}{(K+Z)^{1/4}} \mathrm{e}^{\epsilon^{-1/2}(k_*\Delta)^{1/2}\left(-\mathrm{i}J(k_*\Delta)^{-1}\sqrt{1+\nu_*^2}\sqrt{2(K+Z)}+\mathrm{i}KX\right)} \mathrm{d}K, \end{aligned} \tag{A 13}$$

Since the argument of the dominant exponential is purely imaginary, the stationary phase method can be applied in place of the more general saddle-point method. The stationary point is readily found as

$$K_{\mathrm{s}} = \frac{J^2\left(1+\nu_*^2\right)}{2(k_*\Delta)^2 X^2} - Z. \tag{A 14}$$

Using this, the stationary phase approximation of (A 13) is found as

$$\begin{aligned} w_1 \doteq {} & \frac{\mathrm{i}hfJ^{1/2}\left(1+\nu_*^2\right)^{1/4}\left((k_*\Delta)^2\mathrm{Ro}^2-1\right)^{1/4}}{(k_*\Delta)^{1/2}} \mathrm{e}^{-\left(y-J\nu_* k_*^{-1}(1+\nu_*^2)^{-1/2}D_{\mathrm{II}}\right)^2/(2\Delta^2)} \\ & \times \mathrm{e}^{-\left(a^2/X^2-Z\right)^2/2} \mathrm{e}^{-\mathrm{i}(k_*\Delta)^{1/2}\left(J^2(1+\nu_*^2)/(2(k_*\Delta)^2X)+ZX\right)} \end{aligned} \tag{A 15}$$

where

$$X = \left(k_*(k_*\Delta)^{-3/2}x - J(k_*\Delta)^{-3/2}\left(\sqrt{1+\nu_*^2}\frac{(k_*\Delta)\mathrm{Ro}}{\sqrt{(k_*\Delta)^2\mathrm{Ro}^2-1}} + \frac{\nu_*^2}{\sqrt{1+\nu_*^2}} D_{\mathrm{II}}\right)\right), \tag{A 16}$$

a is defined in (3.42), and we have ignored the rapidly varying phase and have set $\epsilon = 1$.

Appendix B. EP flux at the ground

To obtain the integrated EP flux at the bottom of the domain, we use that

$$\overline{F}_{\rm tot} = 4\pi^2 \int\int F(\boldsymbol{k})\,{\rm d}k{\rm d}l, \tag{B 1}$$

where $F(\boldsymbol{k})$ on the right-hand side is the plane-wave expression for the EP flux in (4.7) and the factor $4\pi^2$ arises in the transformation of the surface integral into a Fourier integral. The form of $F(\boldsymbol{k})$ is dominated by its first term; further, it follows from (3.16) that

$$\hat{w}_\zeta \sim -{\rm i}\frac{J\sqrt{1+\nu^2}}{\sqrt{\zeta^2-1}}\hat{w}. \tag{B 2}$$

The integrated EP flux is therefore approximated as

$$\begin{aligned}\overline{F}_{\rm tot} &= \frac{4\pi^2 J\Lambda\sqrt{\zeta_{\rm b*}^2-1}}{f\zeta_{\rm b*}^2\sqrt{1+\nu_*^2}}\iint |w(\boldsymbol{k})|^2\,{\rm d}k{\rm d}l = \frac{4\pi^2 J\Lambda\sqrt{\zeta_{\rm b*}^2-1}}{f\zeta_{\rm b*}^2\sqrt{1+\nu_*^2}}\frac{k_*^2U_{\rm b}^2h^2\Delta^4}{4\pi^2}\frac{\pi}{\Delta^2}\\ &= \frac{\pi J\Delta^2\Lambda h^2 f\left((k_*\Delta)^2{\rm Ro}^2-1\right)^{1/2}}{(1+\nu_*^2)^{1/2}},\end{aligned} \tag{B 3}$$

in agreement with (4.18).

REFERENCES

Alexander, M. J., Geller, M., McLandress, C., Polavarapu, S., Preusse, P., Sassi, F., Sato, K., Eckermann, S., Ern, M., Hertzog, A., Kawatani, Y., Pulido, M., Shaw, T. A., Sigmond, M., Vincent, R. & Watanabe, S. 2010 Recent developments in gravity-wave effects in climate models and the global distribution of gravity-wave momentum flux from observations and models. *Quart. J. R. Met. Soc.* **136** (650), 1103–1124.

Andrews, D. G. & McIntyre, M. E. 1976 Planetary waves in horizontal and vertical shear: the generalized Eliassen-Palm relation and the mean zonal acceleration. *J. Atmos. Sci.* **33**, 2031–2048.

Andrews, D. G. & McIntyre, M. E. 1978 Generalized Eliassen-Palm and Charney-Drazin theorems for waves on axisymmetric mean flows in compressible atmospheres. *J. Atmos. Sci.* **35**, 175–185.

Booker, J. R. & Bretherton, F. P. 1967 The critical layer for internal gravity waves in a shear flow. *J. Fluid Mech.* **27**, 513–539.

Boyd, J. P. 1976 The noninteraction of waves with the zonally averaged flow on a spherical earth and the interrelationships on eddy fluxes of energy, heat and momentum. *J. Atmos. Sci.* **33**, 2285–2291.

Bretherton, F. 1969*a* On the mean motion induced by internal gravity waves. *J. Fluid Mech.* **36**, 758–803.

Bretherton, F. P. 1966 The propagation of groups of internal gravity waves in a shear flow. *Quart. J. Roy. Meteor. Soc.* **92**, 466–480.

Bretherton, F. P. 1969*b* Momentum transport by gravity waves. *Quart. J. Roy. Meteor. Soc.* **95**, 213–243.

Charney, J. G. & Drazin, P. G. 1961 Propagation of planetary-scale disturbances from the lower into the upper atmosphere. *J. Geophys. Res.* **66**, 83–109.

Edmon, Jr., H. J., Hoskins, B. J. & McIntyre, M. E. 1980 Eliassen-Palm cross sections for the troposphere. *J. Atmos. Sci.* **37**, 2600–2616.

Eliassen, A. & Palm, E. 1961 On the transfer of energy in stationary mountain waves. *Geopy. Publ.* **22**, 1–23.

Fritts, D. C. & Alexander, M. J. 2003 Gravity wave dynamics and effects in the middle atmosphere. *Rev. Geophys.* **41**, 1003.

671 Hasha, A., Bühler, O. & Scinocca, J. 2008 Gravity wave refraction by three-dimensionally
672 varying winds and the global transport of angular momentum. *J. Atmos. Sci.* **65**, 2892–
673 2906.
674 Jones, W. L. 1967 Propagation of internal gravity waves in fluids with shear flow and rotation.
675 *J. Fluid Mech.* **30**, 439–448.
676 Lott, F., Millet, C. & Vanneste, J. 2015 Inertia-gravity waves in inertially stable and
677 unstable shear flows. *J. Fluid Mech.* **775**, 223–240.
678 Lott, F., Plougonven, R. & Vanneste, J. 2010 Gravity waves generated by sheared potential
679 vorticity anomalies. *J. Atmos. Sci.* **67**, 157–170.
680 Lott, F., Plougonven, R. & Vanneste, J. 2012 Gravity waves generated by sheared three-
681 dimensional potential vorticity anomalies. *J. Atmos. Sci.* **69**, 2134–2151.
682 Martin, A. & Lott, F. 2007 Synoptic responses to mountain gravity waves encountering
683 directional critical levels. *J. Atmos. Sci.* **64**, 828–848.
684 Nikurashin, M. & Ferrari, R. 2011 Global energy conversion rate from geostrophic flows
685 into internal lee waves in the deep ocean. *Geophys. Res. Lett.* **38**, L08610.
686 Nikurashin, M. & Ferrari, R. 2013 Overturning circulation driven by breaking internal waves
687 in the deep ocean. *Geophys. Res. Lett.* **41**, 3133–3137.
688 Scott, R. B., Goff, J. A., Garabato, A. C. Naveira & Nurser, A. J. G. 2011 Global
689 rate and spectral characteristics of internal gravity wave generation by geostrophic flow
690 over topography. *J. Geophys. Res.* **116**.
691 Shutts, G. 1995 Gravity-wave drag parametrization over complex terrain: The effect of critical-
692 level absorption in directional wind-shear. *Quart. J. Roy. Meteor. Soc.* **121**, 1005–1021.
693 Shutts, G. 2001 A linear model of back-sheared flow over an isolated hill in the presence of
694 rotation. *J. Atmos. Sci.* **58**, 3293–3311.
695 Shutts, G. 2003 Inertia gravity wave and neutral Eady wave trains forced by directionally
696 sheared flow over isolated hills. *J. Atmos. Sci.* **60**, 593–606.
697 Yamanaka, M. D. & Tanaka, H. 1984 Propagation and breakdown of internal inertio-gravity
698 waves near critical levels in the middle atmosphere. *J. Meteor. Soc. Japan* **62**, 1–16.